Friedrich-Wintgen bound states in the continuum and induced resonances in a loop laterally coupled to a waveguide

Madiha Amrani [1], Soufyane Khattou [1], El Houssaine El Boudouti [1,*], Abdelkrim Talbi [2], Abdellatif Akjouj [3], Leonard Dobrzynski [3], and Bahram Djafari-Rouhani [3]

[1]*LPMR, Département de Physique, Faculté des Sciences, Université Mohammed I, Oujda, Morocco*
[2]*Univ. Lille, CNRS, Centrale Lille, ISEN, Univ. Valenciennes, UMR 8520, IEMN, LIA LICS/LEMAC, F-59000 Lille, France*
[3]*IEMN, UMR CNRS 8520, Département de Physique, Université de Lille, 59655 Villeneuve d'Ascq, France*

The concept of bound states in the continuum (BICs) in a simple cavity attracts much interest in recent works in wave physics. The BICs are perfectly confined modes with an infinite lifetime that reside inside the continuous spectrum of radiative modes, but they remain totally decoupled from it. There exist several types of BICs based on their physical origin: one of the most interesting types is Friedrich-Wintgen (FW) BICs which result from the destructive interference of two resonant modes belonging to the same cavity. Here, we investigate theoretically and experimentally the existence of FW BICs in a side-coupled loop. The cavity is made of a loop of length $2d = d_2 + d_3$ connected to a stub of length d_4. The whole cavity is attached vertically to two semi-infinite waveguides by a wire of length d_1. We demonstrate that the BICs can be induced either by the loop-stub system or by the two arms of lengths d_2 and d_3 of the loop for specific geometrical parameters. When a perturbation in the system produces a deviation from the BIC condition, the latter transforms to either electromagnetically induced transparency (EIT) or reflection (EIR) or Autler-Townes splitting (ATS) resonances. Both EIT and ATS exhibit similar features in the transmission spectrum, namely, a transparency window; however, they have different physical origins. Therefore, EIT and ATS resonances are fitted with corresponding analytical model expressions, revealing good agreements. The Akaike's information criterion is then used to quantitatively discern EIT from ATS and the transition from ATS to EIT is also carried out. Our theoretical results are obtained by means of the Green's function method which enables us to obtain the transmission and reflection coefficients, dispersion relations, as well as density of states and scattering matrix. An experimental validation of all these results is performed in the radio-frequency domain using coaxial cables.

I. INTRODUCTION

Various physical mechanisms of wave trapping and confinement are exploited to improve the performance of physical devices, which can be achieved by using high-quality (Q) factor responses. A more attractive way to trap waves is to use destructive interference in different kinds of physical systems [1]. This mechanism refers to the physics of bound states in the continuum (BICs) [2]. BICs are peculiar modes perfectly localized with no radiation yet lying inside the continuous spectrum of unbounded modes. According to the theory, these modes can be regarded as resonances with an infinite radiative Q factor (i.e., zero width). The first proposal of BICs was due to Von Neumann and Wigner in 1929 for quantum systems [2]. To date, BICs represent an ubiquitous phenomenon applying to all domains of wave physics, such as acoustics [3–10], mesoscopics [11,12], photonics [13–15], and plasmonics [16–18]. There are numerous realizations of BICs in classical systems, leading to a wide variety of different applications such as lasers [19], filters [20,21], demultiplexers [22], and sensors [23,24]. In accordance with the classification presented in

review [25], BICs can be categorized into several types based on their physical origin. Among them, one can cite symmetry-protected (SP) BICs [26–28], Fabry-Perot (FP) BICs [29], and Friedrich-Wintgen (FW) BICs [30] which have been actively investigated recently [10,29,31–40]. SP BICs occur when a system presents modes with symmetry incompatibility, then it is possible to find a bound state of one symmetry class which falls in the continuous spectrum of another symmetry class without any coupling between them [26–28]. FP BICs arise when the resonance frequencies or the spacing between two resonant structures are tuned to make the round-trip phase shift add up to an integer multiple of 2π. This structure is equivalent to a FP cavity created between two resonant reflectors [10,29,31–34]. FW BICs are formed when two resonances, belonging to the same cavity, fall near to each other as a function of a continuous parameter, then interference induces an avoided crossing of the resonances and at one specific set of the parameters, one resonance entirely vanishes and therefore becomes a FW BIC. The other resonance becomes more lossy due to the constructive interference [33–40]. Due to the properties of these BICs, their realization remains elusive in one-dimensional photonic systems [41].

In practice, the BIC does not interact with the surrounding media, therefore, in order to be identified, it is necessary

---

*Corresponding author: elboudouti@yahoo.fr

to make some physical modifications for different devices supporting the BIC. For instance, by introducing specific external or geometrical and material perturbations, a BIC can be coupled with unbounded modes and becomes a leaky mode. Therefore, a small detuning from the BIC condition leads to the transformation of a BIC to either a Fano resonance in the vicinity of an antiresonance (transmission zero), or an electromagnetically induced transparency (EIT) resonance when it falls between two transmission zeros, or an electromagnetically induced reflection (EIR) when it falls between two reflection zeros [11,25]. Conversely, Fano, EIT, and EIR resonances collapse at particular frequencies and geometrical parameters of the system giving rise to BICs; at the frequency of the BIC, the transmission can take a zero or a nonzero value depending on the specific problem. Let us briefly recall here the concepts of Fano, EIT, and EIR resonances. Fano resonance is characterized by an asymmetric line profile resulting from the interaction between two different resonances of different quality factors or the destructive interference between a discrete state and a continuum background [42,43]. Whereas, EIT is originating from an interference phenomenon where a narrow transparency window is created by eliminating a resonant absorption [44]. Similarly, EIR refers to the formation of a reflection window inside a transparency band of a system. Also, another physical phenomenon, known as Autler-Townes splitting (ATS), can exhibit similar features as EIT in the transmission spectrum [45]. Instead of being due to the destructive quantum interference effect, it is caused by strong-field-driven interactions leading to the splitting of energy levels [46]. In essence, both EIT and ATS generate a transparency window but the mechanisms behind them are entirely different, one being a quantum destructive interference and the other a linear alternating current (AC) Stark effect [46]. The similarity between their spectral feature attracts much confusion and discussion on the distinction between EIT and ATS, thus, it is becoming an active topic of research in classical systems [47–50]. Since Anisimov *et al.* [51] first proposed an objective method based on Akaike's information criterion (AIC) to distinguish the regime where EIT or ATS dominates in experimental data, this method has been successfully applied for discerning both mechanisms in various systems such as cold cesium atom [52], hot molecules [53], whispering-gallery-mode microresonators [46], plasmonic waveguides and coupled resonators [54–56], and acoustic and photonic systems [57–59].

Generally, FW BICs have been intensively studied both theoretically and experimentally in regular photonic crystals without [38,60,61] and with [41] an anisotropic defect layer, metasurfaces [37,62–64], and grating systems [40,65,66]. In addition to SP BICs observed at Γ point in the Brillouin zone, FW BICs are observed at off-Γ points in regions of the band dispersion with an accidental symmetry. These regions are attributed to the coupling strength of two radiative modes that interfere destructively and result in extremely high-Q factors around the FW BIC, called supercavity resonances [1,63,64] or near-BIC [40]. Some attempts have been performed to show the possibility to realize FW BICs in a single supercavity. Bogdanov *et al.* [35] have studied strong coupling between modes of a single-subwavelength high-index dielectric resonator to enhance the high-Q factor of the cavity by use of

avoided crossing of resonances but without reaching a true BIC as the width of the supercavity mode cannot turn to zero. Similar results are found by Solodovchenko *et al.* [36] a in finite cylindrical dielectric resonator by the anticrossing of the two resonant modes $TE_{1,1,0}$ and $TM_{1,1,1}$. These simple structures can present an advantage in comparison with periodic structures as they require just one cavity instead of periodic cavities. In this work, we propose a simple cavity [Fig. 1(a)] that displays FW-type BICs that transform into either EIT, EIR, or ATS resonances when the system deviates from the BICs conditions under a small structural perturbation. The proposed system can be transposed to plasmonic devices based on metal-insulator-metal (MIM waveguides), which are suitable for designing efficient refractive sensor at the nanoscale [22]. The cavity is composed of a loop of length $2d = d_2 + d_3$ connected to a wire of length d_1 and a stub of length d_4,; the whole cavity is attached vertically to a waveguide at the bottom side of the wire of length d_1 [Fig. 1(a)]. The boundary condition at the end of the stub is $H = 0$ (i.e., vanishing magnetic field). We demonstrate that these BICs are common eigenmodes of both closed cavities in Figs. 1(b) and 1(c) with Dirichlet and Neumann boundary conditions at the bottom side of the wire, respectively (hereafter called DBCS and NBCS, respectively). We derive closed-form expressions for the geometrical parameters which enables to predict analytically and graphically the locations of these BICs. Indeed, we demonstrate that the BICs are independent of the wire d_1 and additionally originate from (i) the loop-stub system independently of the subdivision of $2d$ into d_2 and d_3, (ii) the modes of the loop if d_2 and d_3 are commensurate with each other, independently of the stub d_4. EIT and ATS phenomena are first fitted, respectively, with the corresponding analytical expressions provided in Refs. [46,52,67] where the difference between both phenomena is highlighted. Also, we display an Akaike's information criterion (AIC) to discern EIT or EIR from ATS resonances. Our study is developed through an analysis of the transmission and reflection coefficients, dispersion relations, and density of states (DOS) using the Green's function method [68]. A comparison between DOS and the derivative of the argument of the determinant of the scattering matrix (the so-called Friedel phase [69]) is also provided. An experimental validation of all these results is performed in the radio-frequency domain using coaxial cables [Fig. 1(d)].

The rest of the paper is organized as follows: In Sec. II, we give a brief review of the method of calculation based on the Green's function approach. We provide the analytical expressions of the dispersion relation of FW BICs, the transmission and reflection coefficients, as well as the DOS and scattering matrix. Also, we give the FW formalism and its application to our system. In Secs. III and IV, we give an analytical and experimental evidence about the existence of FW BICs and their transformation to EIT, EIR, and ATS resonances. The conclusions are presented in Sec. V.

II. THEORETICAL MODEL AND ANALYTICAL RESULTS

The photonic structure presented in Fig. 1(a) is composed by a loop made of two wires of lengths d_2 and d_3 and a stub of length d_4 grafted along the loop of length $2d = d_2 + d_3$. This
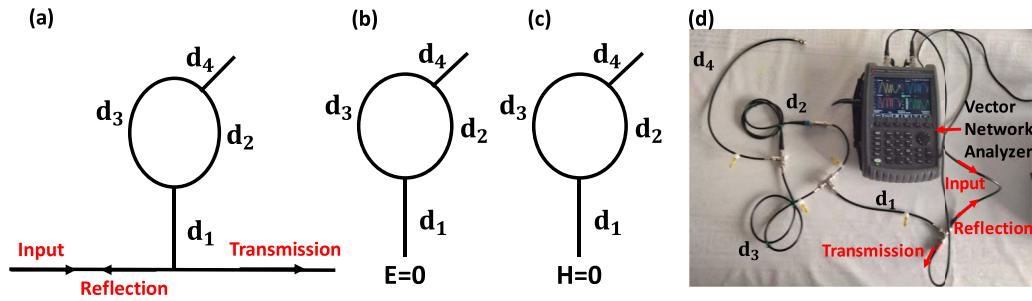
FIG. 1. (a) Schematic representation of the studied system composed of a loop of length $2d = d_2 + d_3$ and a stub of length d_4 coupled to the horizontal waveguide by a wire of length d_1. The whole system is inserted between two semi-infinite waveguides. (b), (c) Loop of length $2d = d_2 + d_3$ and a stub of length d_4 attached to a wire of length d_1 with Dirichlet ($E = 0$) (b) and Neumann ($H = 0$) (c) boundary conditions at the bottom side of the system. (d) Experimental measurement of the transmission and reflection using standard coaxial cables and a vector network analyzer.

loop-stub structure is attached by a wire of length d_1 to two semi-infinite waveguides. The boundary condition at the end of the stub of length d_4 is $H = 0$ (i.e., vanishing magnetic field). All wires and waveguides are characterized by the same impedance Z and dielectric constant ε but with different lengths. The method of calculation used in this study is based on the Green's function approach [68], called interface response theory of continuous media, used to solve the problem of the propagation of electromagnetic waves in a structure with different connection points [Fig. 1(a)]. This method enables us to obtain different physical properties of the studied system such as the transmission and reflection coefficients, dispersion relations, and DOS. Among these properties, one can also cite the eigenmodes of the closed cavities in Figs. 1(b) and 1(c) called as DBCS and NBCS, respectively.

A. Transmission and reflection coefficients and eigenmodes of DBCS and NBCS

The transmission and reflection coefficients for the structure depicted in Fig. 1(a) can be written, respectively, as follows (see the details of the calculation in the Supplemental Material SM1 [70]):

$$t = \frac{\tau}{\tau + j\rho} \tag{1}$$

and

$$r = \frac{-j\rho}{\tau + j\rho}, \tag{2}$$

where

$$\tau = 2S_1 S[2SC_4 + S_4C] + C_1[S_2 S_3 S_4 - 2C_4 SC] \tag{3}$$

and

$$\rho = -2C_1 S[2SC_4 + S_4C] + S_1[S_2 S_3 S_4 - 2C_4 SC], \tag{4}$$

and $C_i = \cos(kd_i)$, $S_i = \sin(kd_i)$ $(i = 1, 2, 3, 4)$, $C = \cos(kd)$, $S = \sin(kd)$, $k = \frac{\omega}{c}\sqrt{\varepsilon}$ with $d = \frac{d_2 + d_3}{2}$. ω is the angular frequency, ε is the permittivity of the waveguides, Z is the characteristic impedance, and c is the speed of light in vacuum.

From the expression of t [Eq. (1)] and r [Eq. (2)], one can obtain the transmission and reflection rates, respectively, as

$$T = \frac{\tau^2}{\tau^2 + \rho^2} \tag{5}$$

and

$$R = \frac{\rho^2}{\tau^2 + \rho^2}. \tag{6}$$

In the absence of dissipation, the conservation energy law $T + R = 1$ can be obtained straightforwardly.

In a previous work [71], we have shown that the eigenmodes of an isolated system with either vanishing electric field ($E = 0$) called Dirichlet boundary condition structure (DBCS) [Fig. 1(b)] or vanishing magnetic field ($H = 0$) called Neumann boundary condition structure (NBCS) [Fig. 1(c)] can be obtained, respectively, from the transmission and reflection zeros when this system is coupled to a waveguide as in Fig. 1(a) (see the Supplemental Material SM1 [70]). Therefore, from the expressions of t and r [Eqs. (1) and (2)], one can deduce the eigenmodes of the DBCS and NBCS, respectively, as

$$\tau = 0 \tag{7}$$

and

$$\rho = 0. \tag{8}$$

Equations (7) and (8) show that the eignemodes of the DBCS and NBCS depend on the lengths d_1, d_2, d_3, and d_4 of the four wires constituting the wire-loop-stub system. In what follows, we will discuss different cases showing BICs according to the choice of the geometrical parameters constituting the whole cavity connected to the semi-infinite waveguides.

B. Conditions for BIC states

In addition to the eigenmodes of the isolated cavities in Figs. 1(b) and 1(c) [Eqs. (7) and (8)], the eigenmodes of the whole structure depicted in Fig. 1(a) are given by the poles of the Green's function or equivalently by the denominator of the transmission and reflection [Eqs. (1) and (2)] coefficients, namely,

$$\tau + j\rho = 0. \tag{9}$$

The latter equation is a complex quantity. Its real part gives the position of the resonances in the transmission spectra and the DOS, whereas its imaginary part is related to the width of the resonance. However, if the real (i.e., τ) and imaginary (i.e., ρ) parts vanish at the same frequency, this will correspond to a bound state falling in a continuum of states. These results clearly show that the BICs [Eq. (9)] are common modes of DBCS [Eq. (7)] and NBCS [Eq. (8)]. From an analysis of Eqs. (3) and (4), one can deduce two types of solutions that are both independent of d_1, namely, the BICs induced by the loop-stub structure and the BICs induced by the two arms of the loop. The latter are also independent of d_4. By adding and subtracting Eqs. (3) and (4) after multiplying them, respectively, by S_1 and C_1, one can easily obtain a first solution of these equations as

$$S[2SC_4 + S_4C] = 0 \tag{10}$$

and

$$S_2S_3S_4 - 2C_4SC = 0. \tag{11}$$

One can note that the BIC conditions, namely, simultaneous vanishing of Eqs. (3) and (4), are independent of length d_1. However, we shall see later the essential role of d_1 for the behavior of the transmission and reflection spectra around the FW BIC. It is worth noting that Eqs. (10) and (11) correspond, respectively, to the eigenmodes of the loop of length $d_2 + d_3$ in contact with the stub of length d_4 with Dirichlet and Neumann boundary conditions at the bottom side of the loop where d_2 and d_3 are attached. After straightforward algebraic calculations, one can get four types of solutions from Eqs. (10) and (11) where the first three solutions depend on d_4 whereas the fourth one is independent of d_4:

(a1)

$$S = 0 \text{ and } S_4 = 0, \tag{12}$$

i.e., $kd = m\pi$ and $kd_4 = m_4\pi$, where m and m_4 are integers with $m \neq 0$. This implies that d_4 and $d = \frac{d_2+d_3}{2}$ are commensurate (i.e., $\frac{d_4}{d} = \frac{m_4}{m}$) whatever the values of d_1, d_2, and d_3.

(a2)

$$C = 0, \ C_4 = 0, \text{ and } S_2 = 0 \text{ (or } S_3 = 0), \tag{13}$$

i.e., $kd = \frac{(2m+1)\pi}{2}$ and $kd_4 = \frac{(2m_4+1)\pi}{2}$, $kd_2 = m_2\pi$, $kd_3 = m_3\pi$, and m_2, m_3 are nonzero integers with $m_2 + m_3 = 2m + 1$ or equivalently d_2 and d_3 are commensurate such that $\frac{d_2}{d_3} = \frac{m_2}{m_3}$ where m_2 and m_3 are of different parities. Also, d_4 and d are commensurate such that $\frac{d_4}{d} = \frac{2m_4+1}{2m+1}$.

(a3)

$$k(d_2 - d_3) = (2n + 1)\pi \text{ and } \tan(kd_4) = -2 \tan(kd), \tag{14}$$

where n is an integer.

(b) In addition to the solutions induced by the loop stub, there is another solution induced by the two arms of lengths d_2 and d_3 of the loop, namely,

$$S = 0 \text{ and } S_2 = 0 \text{ (or } S_3 = 0), \tag{15}$$

i.e., $kd = m\pi$, $kd_2 = m_2\pi$, $kd_3 = m_3\pi$, and m_2, m_3 are nonzero integers with $m_2 + m_3 = 2m$ or equivalently d_2 and d_3 are commensurate such that $\frac{d_2}{d_3} = \frac{m_2}{m_3}$ where m_2 and m_3 are both odd or both even. In this case, Eqs. (3) and (4) vanish

simultaneously giving rise to BIC whatever the values of d_1 and d_4.

C. Density of states and Friedel phase

Another important quantity that enables to deduce the distribution and the weight of the different states in the system is the DOS. The Green's function approach allows us to determine the variation of the DOS [$\Delta n(\omega)$] of the present system and the original uncoupled systems such as [68]

$$\Delta n(\omega) = \frac{1}{\pi} \frac{d}{d\omega} \left[\arctan\left(\frac{\tau}{\rho}\right) \right]. \tag{16}$$

The details of the calculation are given in the Supplemental Material SM1 [70].

In addition to the study of the transmission and reflection coefficients, an interesting complementary quantity that enables to determine other information on the scattering parameters such as the Friedel phase [69] is the scattering matrix S, namely,

$$S = \begin{pmatrix} r & t \\ t & r \end{pmatrix}, \tag{17}$$

where t and r are the transmission and reflection coefficients given by Eqs. (1) and (2), respectively.

Indeed, we first provide an exact analytical comparison between the DOS and the Friedel phase defined as [69] $\theta_f = \text{Arg}[\det(S)]$ for a lossless system. Then, we shall see numerically and experimentally the effect of the loss on such relationship. The determinant of the scattering matrix S for the cavity is given by

$$\det(S) = r^2 - t^2 = \frac{\tau^2 + \rho^2}{(\rho - j\tau)^2}. \tag{18}$$

Therefore, for the lossless system, the scattering Friedel phase can be written as

$$\theta_f = \text{Arg}[\det(S)] = 2 \arctan\left(\frac{\tau}{\rho}\right). \tag{19}$$

Hence, on can deduce from Eqs. (16) and (19) that the DOS is related to the Friedel phase [69] as

$$\frac{d\theta_f}{d\omega} = 2\pi \, \Delta n(\omega). \tag{20}$$

Equation (20) shows that the DOS can be measured indirectly from the measurement of the phase of $\det(S)$. One can notice that for the lossless system, we can easily check the well-known relation $|\det(S)| = 1$. Also, for a lossy system, the analytical equation (20) is no longer valid when $\det(S)$ tends to zero, and therefore $\frac{d\theta_f}{d\omega}$ exhibits a different behavior in comparison with the DOS. It is worth noting that Eq. (20) has been obtained in mesoscopic systems in absence of loss [72,73], however, there are few works on such relationship in the presence of loss [62,74–79]. In addition, most of the theoretical demonstrations assume that the systems are lossless [62,76,77] which hide interesting additional information when $\det(S)$ is close to zero. Recently, we have given a detailed comparative study of the DOS and scattering parameters for lossless and lossy photonic systems [79].

D. Friedrich-Wintgen BIC formalism

In the next section, we will show that FW BICs occur at the crossing or anticrossing frequencies of two interacting modes associated to either DBCS or NBCS. Therefore, it is necessary to recall the formalism of FW BICs, which is a special BIC obtained through geometrical and/or material parameters tuning. Unlike the Fabry-Pérot BICs where the resonances are induced by two cavities located at two distant positions along the propagation direction, the resonances leading to FW BICs are located in the same cavity and are coupled to the same radiation channel as it is the case here [25]. In general, the spectral location of the FW BIC occurs near the frequency crossings of the uncoupled resonances. In the two-band model, the Hamiltonian giving the eigenmodes can be written as a generalized eigenvalue problem [25,34]

$$H = \begin{pmatrix} \Omega_1 & \kappa \\ \kappa & \Omega_2 \end{pmatrix} - i \begin{pmatrix} \gamma_1 & \sqrt{\gamma_1\gamma_2} \\ \sqrt{\gamma_1\gamma_2} & \gamma_2 \end{pmatrix}, \qquad (21)$$

where $\Omega_{1,2}$ and $\gamma_{1,2}$ are the resonance frequencies and radiation rates of the uncoupled resonances, respectively. κ is the near-field coupling between the two resonances (or Rabi splitting) and $\sqrt{\gamma_1\gamma_2}$ is the via-the-continuum coupling term since the two resonances interfere and radiate into the same channel. The necessary condition to get one real eigenvalue (Ω_-) of Eq. (21) (i.e., a BIC) and the other eigenvalue called (Ω_+) lossy, can be expressed as [30]

$$\sqrt{\gamma_1\gamma_2}(\Omega_1 - \Omega_2) = \kappa(\gamma_1 - \gamma_2). \qquad (22)$$

When Eq. (22) is satisfied, the two eigenfrequencies, solutions of Eq. (21), can be written as follows [38]:

$$\Omega_- = \frac{\Omega_1 + \Omega_2}{2} - \frac{\kappa(\gamma_1 + \gamma_2)}{2\sqrt{\gamma_1\gamma_2}}, \qquad (23a)$$

$$\Omega_+ = \frac{\Omega_1 + \Omega_2}{2} + \frac{\kappa(\gamma_1 + \gamma_2)}{2\sqrt{\gamma_1\gamma_2}} - i(\gamma_1 + \gamma_2). \qquad (23b)$$

Equations (23a) and (23b) show that at the BIC position, the imaginary part of the complex solution is maximal (i.e., $\gamma_+ = \gamma_1 + \gamma_2$), while the one of the real solution vanishes (i.e., $\gamma_- = 0$). Also, from Eqs. (23a) and (23b), one can get the particular case where the near-field coupling $\kappa = 0$, while the radiation rates γ_1 and γ_2 are different from zero. In this case, Eq. (22) gives $\Omega_1 = \Omega_2 = \Omega_0$ and therefore Eqs. (23a) and (23b) become

$$\Omega_- = \Omega_0, \qquad (24a)$$

$$\Omega_+ = \Omega_0 - i(\gamma_1 + \gamma_2). \qquad (24b)$$

Let us mention that in our structure, the position of the modes (Ω_- and Ω_+) as well as their linewidths (γ_- and γ_+) are obtained from the resonances and antiresonances in the transmission spectra when the cavity is inserted between two semi-infinite waveguides [Fig. 1(a)].

E. FW BIC mechanism in the loop laterally coupled to the waveguide

We have shown that the FW BICs in the loop-stub structure occur at the intersection points between $\tau = 0$ (DBCS) and $\rho = 0$ (NBCS). We give in the Supplemental Material

SM2 [70] different cases showing the solutions of $\tau = 0$ (DBCS) and $\rho = 0$ (NBCS) (i.e., BICs) according to the choice of the geometrical parameters constituting the whole cavity. In the vicinity of BICs, it appears either a second mode of DBCS or second mode of NBCS. The interaction between two DBCS modes or NBCS modes (i.e., two modes belonging to the same cavity) is at the origin of the BICs of FW type. Indeed, for the final system where the cavity is attached to the semi-infinite waveguides [Fig. 1(a)], the width of one mode vanishes when approaching the BIC while the other mode becomes broader and more lossy in analogy with Eqs. (23) and (24) of the FW model. Now, we focus on the FW BICs resulting from the interaction between two modes of DBCS. The solutions of DBCS are given by $\tau = 0$ [Eq. (3)] which after some manipulation can be written in a more appropriate way in relation with the discussions below:

$$\tau = C_1\big\{\big(4S_1^2 C + S_2 S_3\big)S_4 + 2S\big(4S_1^2 - C\big)C_4\big\}$$
$$+ 4S_1(2C_4 S + S_4 C)\cos\left[k\left(\frac{d}{2} + d_1\right)\right]\sin\left[k\left(\frac{d}{2} - d_1\right)\right]. \qquad (25)$$

The frequencies of the two dips and their widths allow us to obtain different parameters of FW model such as the coupling strength (or Rabi splitting) κ and the linewidths of the resonances. In analogy with the FW model, the second term on the right-hand side of Eq. (25) plays the role of the coupling strength κ between the two DBCS modes. Indeed, one can distinguish two cases, namely, the case where $d_1 = \frac{d}{2}$ gives rise to the two decoupled modes (with $\kappa = 0$)

$$C_1 = 0 \qquad (26)$$

and

$$\big(4S_1^2 C + S_2 S_3\big)S_4 + 2S\big(4S_1^2 - C\big)C_4 = 0 \qquad (27)$$

and the case $d_1 \neq \frac{d}{2}$ with $\kappa \neq 0$ (coupled modes).

In what follows, we will give some numerical illustrations with experimental verifications of the BICs induced by (i) the loop-stub structure with coupling ($\kappa \neq 0$) and no-coupling ($\kappa = 0$) regimes (Sec. III) and (ii) the two arms of lengths d_2 and d_3 of the loop (Sec. IV). These two types of BICs can result from the interaction of two modes of DBCS and one NBCS or two modes of NBCS and one DBCS. When we deviate slightly from BICs, we obtain EIT, EIR, and ATS resonances. These two latter cases will be the subject of the two forthcoming sections.

III. BICS AND RESONANCES INDUCED BY THE LOOP-STUB STRUCTURE

As mentioned in Sec. II B, the whole cavity exhibits BICs induced by the loop-stub structure which are independent of d_1. These BICs depend on d_4, $d = \frac{d_2 + d_3}{2}$, and d_2 (or d_3). In what follows, we fix the whole length of the loop (or its half, i.e., d) and investigate the effect of d_2 and d_4 on the BICs as well as their transformation into EIT, EIR, and ATS resonances for given values of d_1. In this section, we shall give the details of a theoretical and experimental evidence of BICs for two given values of d_1 ($d_1 = 0.5d$ and $0.3d$) while choosing $d_2 = 0.2d$ and $d_3 = 1.8d$. We start by treating the
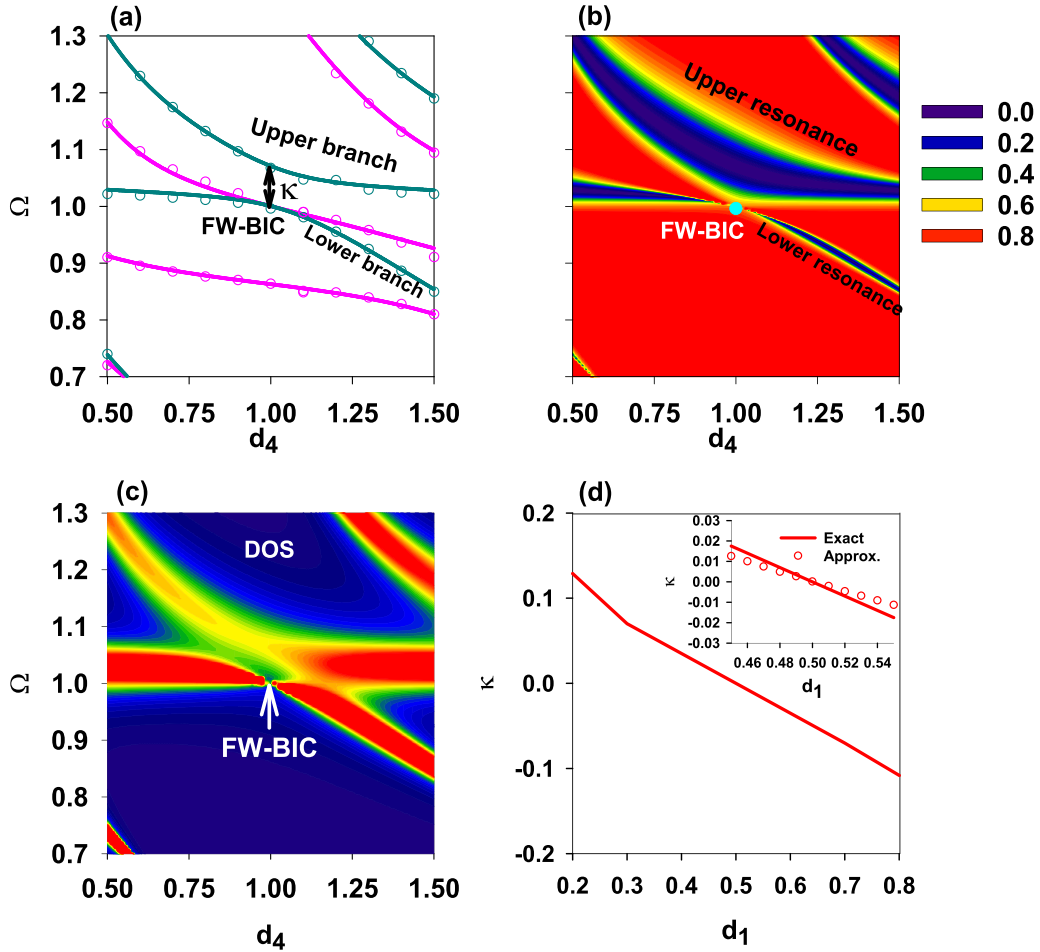
FIG. 2. (a) Dispersion curves of the system depicted in (b) with DBCS ($\tau = 0$, cyan lines) and (c) with NBCS ($\rho = 0$, pink lines) as a function of the length d_4 for $d_1 = 0.3$. The lengths of the arms of the loop are taken such that $d_2 = 0.2$ and $d_3 = 1.8$. Open circles represent the minima of the transmission and reflection spectra obtained by the experimental data. (b) Theoretical variation of the transmission magnitude and (c) DOS in arbitrary units versus Ω and the length of the stub d_4. (d) Rabi splitting κ between the two branches in (a) as a function of d_1. The inset gives a comparison between the exact (solid line) and approximate (open circles) results of κ around $d_1 = 0.5$. The approximate results will be discussed later together with Eq. (28).

BICs given by Eq. (12), namely, when d_4 and d are taken commensurate (i.e., $\frac{d_4}{d} = \frac{m_4}{m}$). These BICs are given by $kd = m\pi$. We shall focus on the BICs falling around $kd = \pi$ (i.e., $m = 1$) and $d_4 = d$ (i.e., $m_4 = 1$). The lengths of the arms of the loop ($d_2 = 0.2d$ and $d_3 = 1.8d$) do not introduce any additional BICs around $kd = \pi$ as the corresponding BICs fall at $kd = 5\pi$ (see Sec. II B). For the sake of simplicity, all lengths will be given in units of $d = 1$ m (half of the length of the loop) and we use the dimensionless frequency $\Omega = \frac{kd}{\pi} = \frac{\omega d \sqrt{\varepsilon}}{\pi c}$. The experiment is performed using a vector analyzer and standard coaxial cables [Fig. 1(d)]. The details of the experimental procedure are given in Ref. [68]. In the calculation, the loss is introduced by adding a complex dielectric constant ($\varepsilon = \varepsilon' + j\varepsilon''$) to match the experimental data. The attenuation coefficient α'' can be expressed as $\alpha'' = \frac{\varepsilon'' \omega}{c \sqrt{\varepsilon'}}$.

A. Coupling regime

As mentioned above [Eq. (25)], in order to get a coupling between the two crossing branches of DBCS, we should take d_1 different from $d_1 = 0.5$. Figure 2(a) shows the dispersion

curves versus d_4 of the DBCS (cyan lines) and NBCS (pink lines) for $d_1 = 0.3$. One can see an avoided crossing behavior around $\Omega = 1$ with a Rabi splitting $\kappa = 0.072$ at $d_4 = 1$ of the two DBCS branches. As predicted, a BIC appears at $\Omega = 1$ when $d_4 = 1$ as the intersection of one DBCS ($\tau = 0$) and one NBCS ($\rho = 0$) branch. In the vicinity of the BIC, one can observe the coupling between two DBCS branches, as required for the FW BIC type. The cyan and pink open circles indicate the experimental data related to the minima and maxima of the transmission coefficient, respectively. The variation of the transmission magnitude (in color scale) versus d_4 is given in Fig. 2(b), demonstrating the noticeable appearance of the anticrossing point around $\Omega = 1$ and $d_4 = 1$. One can observe that the width of lower dip narrows to zero ($\gamma_- = 0$) at $d_4 = 1$, resulting in FW BIC owing to the destructive interference between the two DBCS modes of the cavity. Whereas, the upper dip becomes more lossy ($\gamma_+ = \gamma_1 + \gamma_2 = 0.12$) as shown by the blue color at the anticrossing point [Fig. 2(b)]. This satisfies the FW criterion in Eq. (22). The avoided crossing is due to the strong coupling between the two modes of the cavity. We also notice that the width of the upper mode is

considerably affected by the length d_4, while the width of the lower mode is less affected. However, when we shift from the FW BIC position, one can obtain either EIT or ATS depending on the length d_4 as will be discussed below in Sec. III B. These results are also confirmed in the DOS reported in Fig. 2(c). One can see the shrinking of the lower resonance width leading to a delta peak at the FW BIC position, while the width of the upper mode remains almost constant and is less affected by the length d_4. Let us mention that the Rabi splitting depends significantly on d_1. Hence, we give in Fig. 2(d) the Rabi splitting κ (solid line) versus d_1 around $d_1 = 0.3$. It can be seen that κ changes sign when d_1 goes through 0.5. In other words, when d_1 is below 0.5 and κ is positive, it is the lower DBCS branch that crosses the NBCS branch and they give rise to the FW BIC as shown in Fig. 2(a). On the contrary, for d_1 above 0.5, κ becomes negative and it is the higher DBCS branch that crosses the NBCS branch, while the lower DBCS branch detached from the NBCS branch. At $d_1 = 0.5$, κ is zero and the two DBCS and the one NBCS branches cross each other at the frequency of the BIC. These behaviors are discussed in the Supplemental Material SM2 [70]. In Sec. III B, we will discuss the approximate results displayed in the inset of Fig. 2(d) (open circles) around $d_1 = 0.5$ in the case of no-coupling regime (i.e., $\kappa = 0$) together with an approximate expression [Eq. (28)].

To gain a deeper insight about the behavior of FW BIC, we present in Fig. 3 the transmission magnitude (left panel) and DOS (right panel) versus Ω for different values of d_4. The predicted position of the FW BIC is indicated by the vertical dashed lines in Figs. 3(d) and 3(k). Let us start with the case $d_4 = 0.5$ [Fig. 3(a)]: one can see a broad transparency window squeezed between two dips (indicated by solid and dashed vertical arrows) giving rise to the ATS resonance. Now, when d_4 increases from 0.5 to 0.9 [Figs. 3(b) and 3(c)], the width of the fixed dip (indicated by the solid arrow) around $\Omega = 1$ decreases and the second dip (indicated by the dashed vertical arrow) gets close to the first mode around $\Omega = 1$. Thus, the width of the transparency window decreases giving rise to an asymmetric EIT resonance. For $d_4 = 1$ [Fig. 3(d)], the Friedrich-Wintgen condition is met at $\Omega = 1$, resulting in the collapse of the first dip in the shape of the FW BIC with zero radiation loss ($\gamma_- = 0$). Whereas, the second dip becomes more radiative, its radiation loss becomes the sum of two initial modes $\gamma_+ = \gamma_1 + \gamma_2 = 0.13$. For $d_4 > 1$, the dip around $\Omega = 1$ reappears again at $\Omega < 1$ when d_4 increases as it is shown by the solid arrow in Figs. 3(e)–3(g), while the other mode indicated by the dashed arrow remains almost constant around $\Omega = 1.04$. Similarly to Figs. 3(a) and 3(c), one can obtain EIT or ATS according to the value of $d_4 > 1$ [Figs. 3(e) and 3(g)]. The theoretical (red curves) and experimental (green curves) results are in good agreement. The DOS in Figs. 3(h)–3(n) (right panel) further reveals that the width of the peak at $\Omega \simeq 1$ (indicated by the solid arrow) decreases as far as d_4 tends to 1. For $d_4 = 1$ [Fig. 3(k)], the width of the peak reduces to zero, leading to the formation of a delta peak (FW BIC). Whereas, the second peak (indicated by the dashed arrow) remains broad and its position gets closer to $\Omega = 1$ for $d_4 \simeq 1$. For $d_4 > 1$ [Figs. 3(l)–3(n)], the first peak falls below $\Omega = 1$ when d_4 increases, whereas the upper mode (dashed arrow) remains almost constant at $\Omega = 1.04$.

As mentioned above, the relation between the DOS [Eq. (16)] and the derivative of the Friedel phase [Eq. (19)] is exact for a lossless system [Eq. (20)]. However, the presence of loss affects considerably the above relation. From Figs. 3(h)–3(n), one can see that the DOS is almost similar to $\frac{d\theta_f}{d\omega}$ except at $d_4 = 0.9$ and 1.1 where the derivative of the Friedel phase exhibits a negative delta peak at the quasi-BIC position. Indeed, this can be explained by the fact that $\det(S)$ almost vanishes (i.e., $t \simeq \pm r$) at this position and changes sign, resulting in an abrupt phase change of π in the phase of $\det(S)$ and then a negative delta peak in the derivative of the Friedel phase of θ_f as illustrated in Figs. 3(j) and 3(l). The experimental results of the derivative of the Friedel phase (green open circles) are in good agreement with the theoretical ones in presence of loss (blue dashed lines).

To give an overview of the FWHM of the two dips in Figs. 3(a)–3(g), we display in Fig. 4(a) the linewidth of the lower γ_- (blue line) and upper γ_+ (red line) dips versus d_4. These data are extracted from the resonance peaks in the transmission spectra of the theoretical results in presence of loss. The linewidth of the lower dip decreases as far as d_4 tends to 1 and becomes zero at $d_4 = 1$ resulting in the formation of FW BIC. Whereas, the upper dip increases with d_4 and goes through a maximum ($\gamma_+ \simeq 0.13$) at $d_4 = 1$ and then decreases for $d_4 > 1$. Consequently, the BIC in the lower branch at $d_4 = 1$ coincides with the maximum of the radiative loss in the upper branch. This is in accordance with the loss-exchange mechanism at the FW BIC given in Eq. (22). This is a characteristic of FW BIC, namely, when one of the modes becomes lossless $\gamma_- = 0$, the other mode takes the all losses (γ_+ is maximal). The experimental results (open circles) are well reproduced by the theoretical ones (continuous curves). Figure 4(b) represents the Q factors of the lower (blue lines) and upper (red lines) dips. One can note that the Q factor presents different behaviors for both dips. It depends considerably on the values of d_4. At the BIC position, the Q factor of the lower dip (Q_-) reaches a high value, whereas the Q factor (Q_+) of the upper dip remains fixed around $Q_+ = 10$. It is worth noting that even in presence of loss, the Q factor increases and it goes to infinity when d_4 tends to $d_4 = 1$ as γ_- tends to zero.

In the previous results, we have discussed the modes given analytically by Eq. (12). In this section, we do not discuss further the solutions of Eq. (13) because the physical interpretations are similar to those found with Eq. (12) (see the Supplemental Material SM2 [70]). Now, we focus on the additional BICs obtained graphically by Eq. (14). These modes are independent of the wire of length d_1. Therefore, the length d_1 is fixed to 0.3 and we shall discuss the results around $\Omega = 2$. The dispersion curves of both systems DBCS (cyan lines) and NBCS (pink lines) are illustrated in Fig. 5(a), showing multiple avoided crossings as well as multiple FW BICs at different values of d_4. The coordinates of these anticrossing points fall around ($d_4 = 0.55$ and $\Omega = 1.96$) and ($d_4 = 1.06$ and $\Omega = 1.96$). In the vicinity of these anticrossing points, one can see the intersection of the DBCS and NBCS curves, resulting in the formation of FW BICs. The first BICs labeled I, III, and V are given by Eq. (12) (i.e., $\Omega = 2$ and $d_4 = \frac{m_4}{2}$ where $m_4 = 1, 2, 3$). The BICs marked II and IV (cyan diamond) are obtained graphically from Eq. (14) (i.e., $n = 2$).
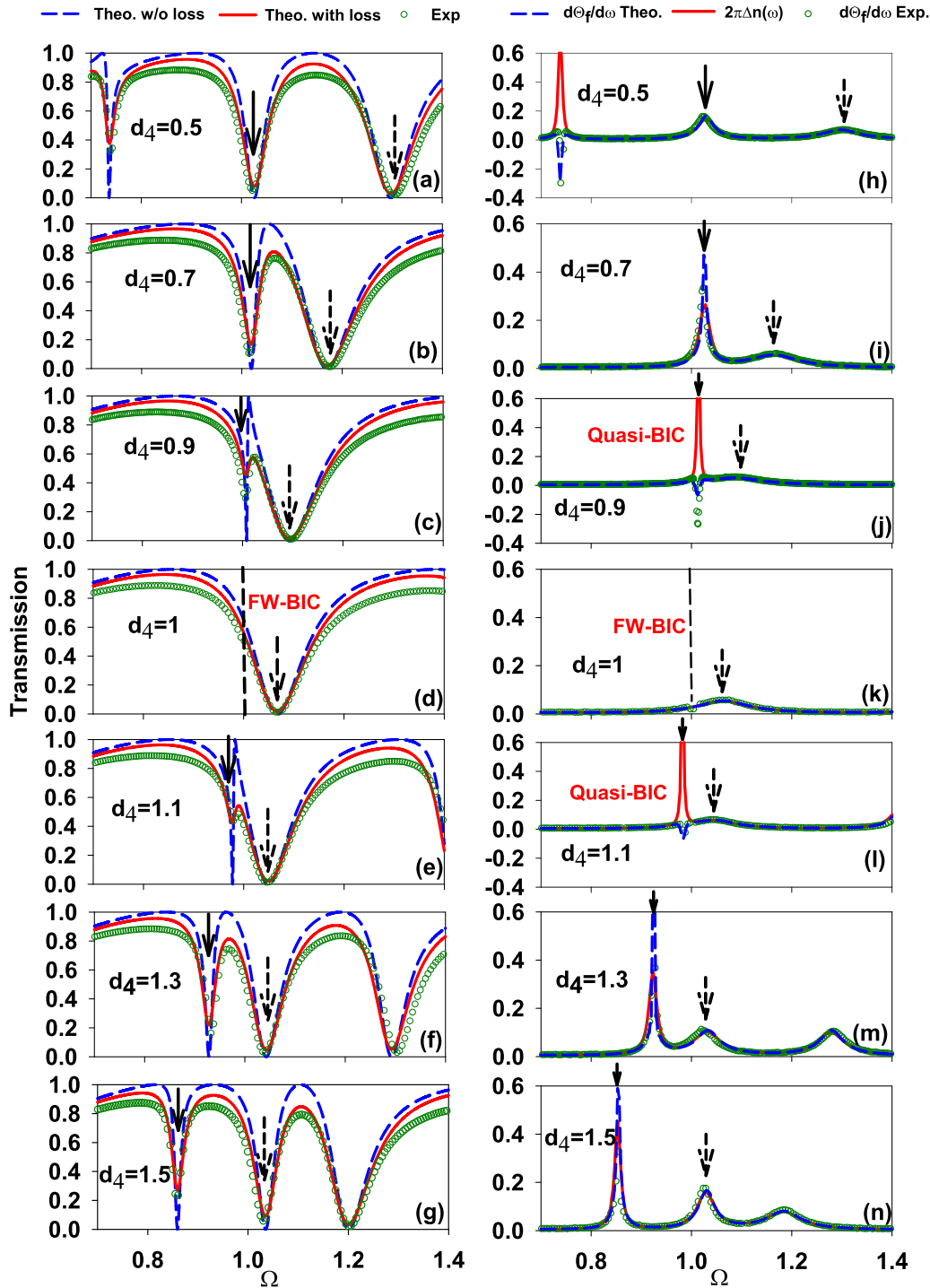
FIG. 3. (a)–(g) (Left panel) Transmission coefficient versus Ω for different values of d_4 around $d_4 = 1$ for $d_1 = 0.3$. The lengths of the arms of the loop are taken such that $d_2 = 0.2$ and $d_3 = 1.8$. Blue and red curves correspond to theoretical results without and with loss, respectively, whereas green curves correspond to experimental results. (h)–(n) (Right panel) Variation of the DOS (red lines) and the derivative of the Friedel phase $\frac{d\theta_f}{d\omega}$ (blue dashed curves) for different values of d_4. The position of FW BIC is indicated by the dashed lines in (d) and (k). The theoretical results of $\frac{d\theta_f}{d\omega}$ (blue dashed lines) are validated by the experimental data (green open circles). The solid and dashed arrows indicate the positions of the transmission dips.

These modes fall, respectively, around $d_4 = 0.65$ and 1.18 at $\Omega = 1.87$. Interestingly, it can be clearly observed that the FW BICs are located in this case in the vicinity of the avoided crossing branches and not at the crossing position itself as in

Fig. 2. The open circles represent the maxima and minima of the transmission coefficient obtained from the experimental data. These results are also confirmed in the variation of the transmission magnitude as shown in Fig. 5(b). To reveal
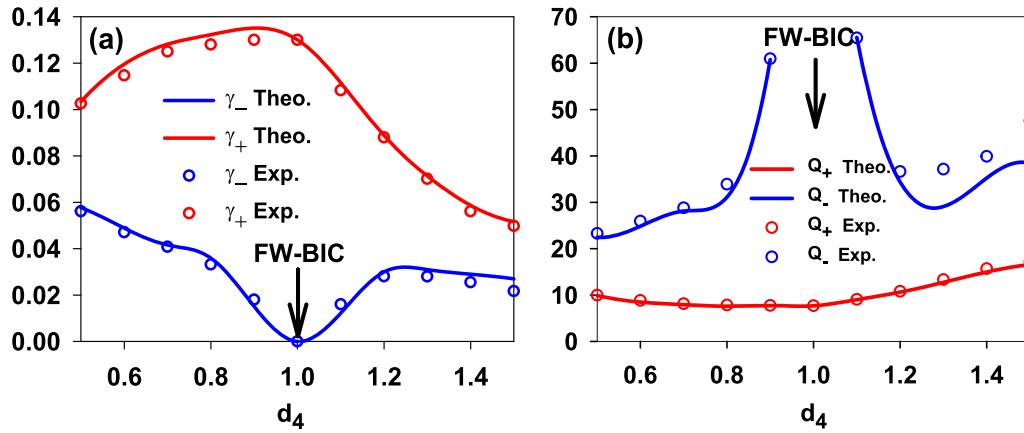
FIG. 4. (a) The radiative linewidth and (b) the quality factor of the lower (blue lines) and upper (red lines) dips indicated by the arrows in Figs. 3(a)–3(g) as a function of the length d_4. Open circles correspond to the experimental data. The black arrows indicate the positions of FW BIC.

more neatly the behavior of these BICs, we focus on the first avoided crossing as given in the inset of Fig. 5(a). In this context, we give in Figs. 5(c)–5(f) the transmission spectra versus Ω for different values of d_4 near $d_4 = 0.5$. One can notice the existence of FW BIC marked I around $\Omega = 2$ indicated by the dashed vertical line in Fig. 5(c) where the width of the first dip vanishes and the transmission rate takes the value $T = 0.3$. For $d_4 = 0.55$ [Fig. 5(d)], the BIC transforms to a quasi-BIC in the lossless transmission spectrum (blue curve). For $d_4 = 0.6$ [Fig. 5(e)] the quasi-BIC still persists and remains robust due to its proximity with the second FW BIC marked II at $d_4 = 0.65$ as shown in Fig. 5(f). Let us note that the BICs I and II are independent of d_1 and between these two BICs, we obtain always quasi-BICs by adjusting the parameter d_4. However, the loss affects considerably these quasi-BICs, which render difficult their detection in the experimental transmission spectra [Figs. 5(d) and 5(e)].

B. No-coupling regime

As can be seen from Eq. (25) for $d_1 = 0.5$, there is a crossing between two branches of DBCS [Eqs. (26) and (27)] at $\Omega = 1$. Figure 6(a) shows the variation of the eigenmodes of the DBCS (cyan lines) and NBCS (pink lines) versus the length d_4 of the stub. The blue horizontal curve at $\Omega = 1$ corresponds to the modes given by $C_1 = 0$ [Eq. (26)], whereas the other cyan branches are given by Eq. (27) of the DBCS. Two branches cross each other at $\Omega = 1$ and $d_4 = 1$ (i.e., $S = 0$ and $S_4 = 0$) since Eq. (27) can easily be factorized by C_1, giving rise to a two-times degenerate mode of DBCS with no coupling $\kappa = 0$ [see Fig. 2(d)]. Also, the condition $S = S_4 = 0$ (Sec. II B) makes the branch associated to NBCS (pink lines) pass also through this frequency $\Omega = 1$, giving rise to a FW BIC [Fig. 6(a)]. When we shift from the crossing point, FW BIC transforms to either EIT or ATS resonances, i.e., a resonance ($\rho = 0$) squeezed between two transmission zeros ($\tau = 0$) (see below). The cyan and pink open circles represent, respectively, the minima of the transmission and reflection coefficients obtained from the experimental spectra (see below). There is a good agreement between the experimental and analytical results.

In order to give a better insight about the behavior of FW BIC, we plot in Figs. 6(b) and 6(d), respectively, the theoretical and experimental variations of the transmission magnitude (in color scale) versus Ω and d_4. One can observe a crossing between the mode of the loop alone [Eq. (26)] at $\Omega = 1$ and the other mode of the cavity [Eq. (27)] with $\kappa = 0$ at $\Omega = 1$ where the FW BIC occurs. More notably, the BIC occurs when one of the two modes is lossless $\gamma_- = 0$, while the other mode is highly lossy with $\gamma_+ = \gamma_1 + \gamma_2 = 2\gamma_1 = 0.1$ [Eq. (24)] and $\Omega_1 = \Omega_2 = \Omega_0 = 1$ as shown in Figs. 6(b) and 6(d). In the vicinity of the crossing point at $\Omega = 1$, the separation between the two modes increases when d_4 deviates from $d_4 = 1$ leading to a narrow transparency window between them as shown in Figs. 6(b) and 6(d). This phenomenon, originating from a destructive interference between the incident wave and the scattered wave by the finite structure, represents what is called EIT resonance. As mentioned previously, this kind of resonance is a consequence of the coupling between the FW BIC induced by the loop and the other modes obtained by loop-wire-stub system. When we shift significantly from $d_4 = 1$, the two modes become very separated from each other around the crossing point ($d_4 = 1$, $\Omega = 1$). Therefore, the transmission dip splits into two dips with a broad transparency window in the middle referred to as the electromagnetic analog of ATS when d_4 is far from $d_4 = 1$. The experimental results [Fig. 6(d)] are in good agreement with the theoretical ones [Fig. 6(b)] in presence of loss. In addition, EIT and ATS as well as BICs can be characterized also by the DOS where these modes appear as resonances with either finite or zero width. Figure 6(c) shows the DOS (with color scale) versus Ω and d_4. One can observe a shrinking of the resonances at the crossing point around $\Omega = 1$ and $d_4 = 1$ giving rise to a delta peak at the BIC (see below). When we shift from the BIC condition, we obtain classical Breigt-Wigner resonances in the DOS (see below). These results are in accordance with those found in the transmission magnitude [Figs. 6(b) and 6(d)].

As mentioned previously [Eq. (25)], the FW BIC did not depend on the length of the wire d_1, however, the coupling strength κ (or Rabi splitting) between the two branches of DBCS [Eq. (25)] depends strongly on d_1 around $d_1 = \frac{1}{2}$.
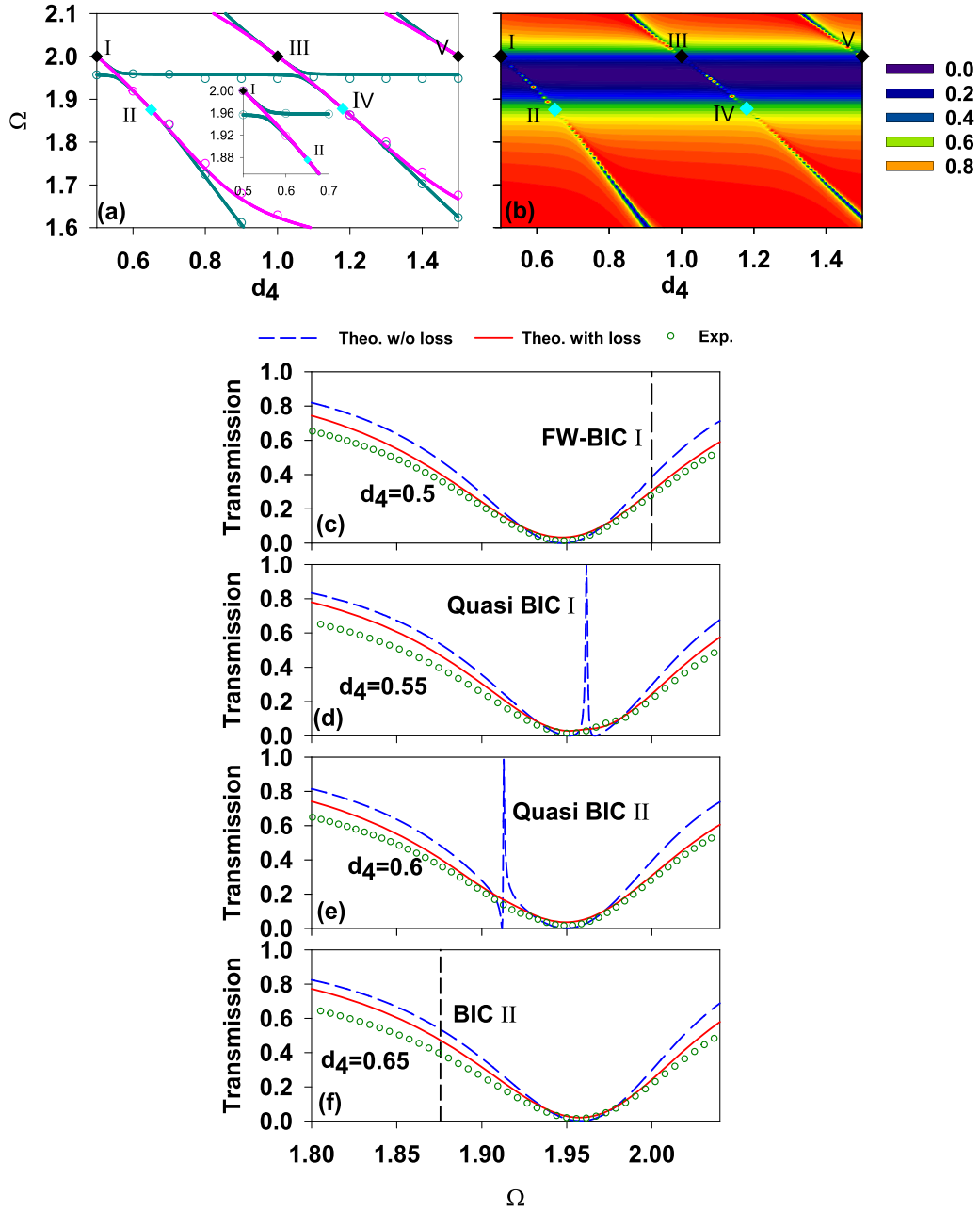
FIG. 5. (a) Dispersion curves of DBCS (cyan lines) and NBCS (pink lines) as a function of d_4 for $d_1 = 0.3$. The black (cyan) diamond indicates the positions of FW BICs marked I, III (II, IV, V). The lengths of the arms of the loop are taken such that $d_2 = 0.2$ and $d_3 = 1.8$. The cyan and pink open circles represent the experimental results obtained from the minima and maxima of the transmission coefficient. (b) Theoretical variation of the transmission magnitude versus Ω and the length of the stub d_4. (c)–(f) Transmission spectra for different values of d_4. Blue and red curves correspond to theoretical results without and with loss, respectively, whereas green circles correspond to the experimental results. The dashed lines in (b) and (e) indicate the positions of FW BICs. The inset in (a) shows a magnification around the first anticrossing at $d_4 = 0.55$.

Therefore, in order to give a quantitative study of this coupling effect close to $d_1 = \frac{1}{2}$ (i.e., $d_1 = \frac{1}{2} + \delta$), we have performed an approximate analytical expression for the Rabi splitting κ. A tedious calculation based on a Taylor expansion of Eq. (25) at $d_4 = 1$ around $\Omega = 1$ (i.e., $\Omega = 1 + \pi\epsilon$ with $\pi\epsilon \ll 1$) enables us to get

$$\kappa = \frac{2\pi[(\pi\Delta^2) - 2]}{\chi_1 - \chi_2 + \chi_3}\delta, \tag{28}$$

where $\chi_1 = 14 - 3(2\pi\delta)^2 - (2\pi\Delta)^2$, $\chi_2 = 2\pi[6\delta(1 + 2\delta) - 2\Delta(1 - 2\Delta)]$, $\chi_3 = 9(2\pi\delta)^2[2\delta + 1] - 24\delta$, and $\Delta = \frac{d_2 - d_3}{2}$.

Equation (28) clearly shows that when $\delta = 0$ (i.e., $d_1 = \frac{1}{2}$) the Rabi splitting κ vanishes, thus, there is no coupling between the two modes of the cavity. Whereas, when δ shifts slightly from 0, κ becomes negative or positive depending on whether $d_1 > \frac{1}{2}$ (i.e., $\delta > 0$) or $d_1 < \frac{1}{2}$ (i.e., $\delta < 0$), respec-
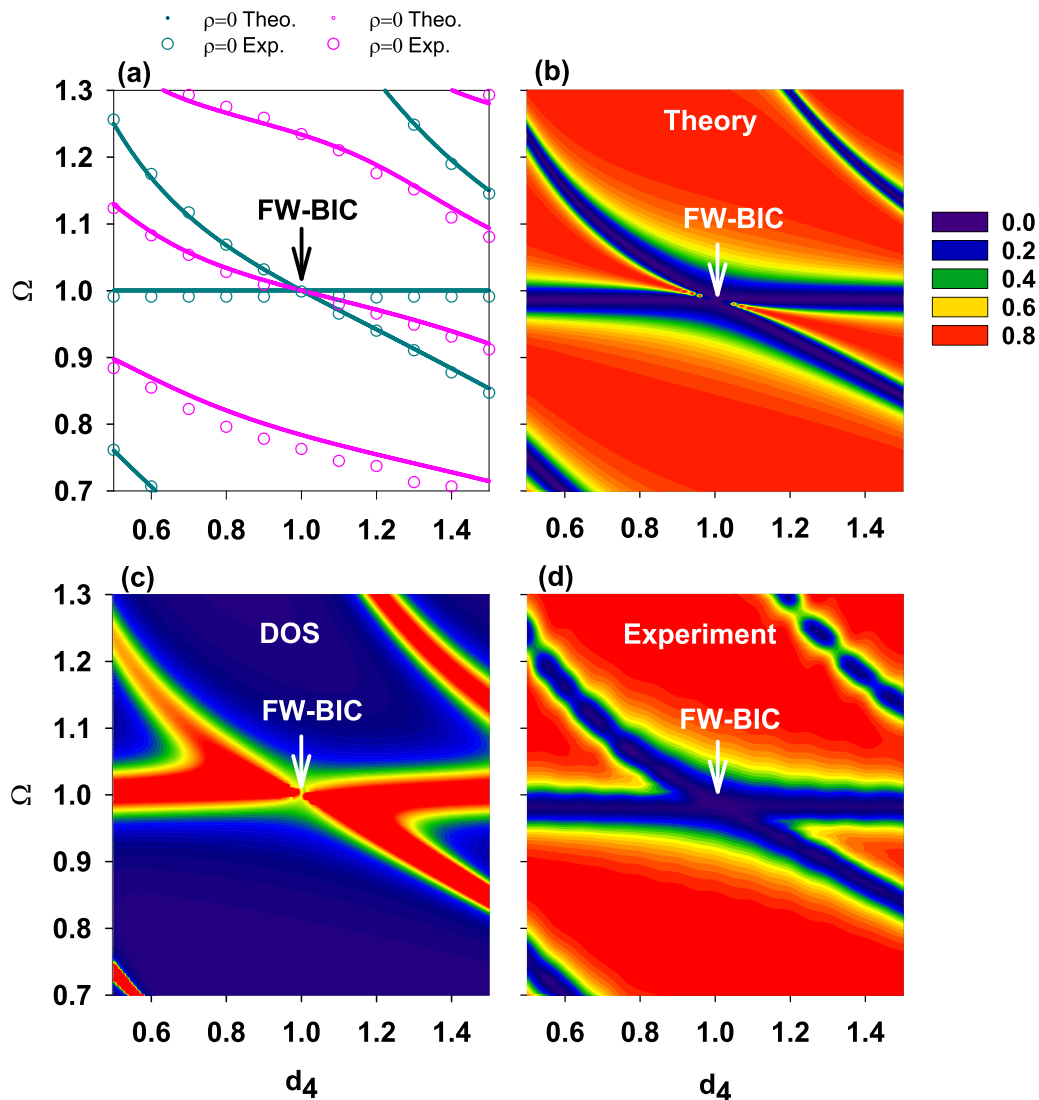
FIG. 6. (a) Dispersion curves of the systems depicted, respectively, in Fig. 1(b) with DBCS ($\tau = 0$, cyan lines) and Fig. 1(c) with NBCS ($\rho = 0$, pink lines) as a function of the length d_4. The lengths of the arms of the loop are taken such that $d_2 = 0.2$ and $d_3 = 1.8$. Cyan and pink open circles represent, respectively, the minima of the transmission and reflection spectra obtained from the experimental data. (b) Theoretical and (d) experimental variation of the transmission magnitude versus Ω and d_4. (c) DOS (in color scale) in arbitrary units versus Ω and d_4.

tively. These results are confirmed in the inset of Fig. 2(d) where we have plotted the exact (red line) and approximate (open circles) results of κ versus d_1 around $d_1 = \frac{1}{2}$. It can be observed that close to $d_1 = \frac{1}{2}$, the exact and the approximate results present a good agreement.

To further visualize the behavior of FW BIC, we plot in Fig. 7 the transmission (left panel) and DOS (right panel) versus Ω for different values of d_4 around $d_4 = 1$. The blue and red curves correspond to the theoretical transmission results without and with loss, respectively, whereas the green circles represent the experimental data. The experimental results show good agreement with the calculated ones. The filled circle on the abscissa of Fig. 7(d) and the dashed line in Fig. 7(k) indicate the position of FW BIC in the transmission and DOS spectra, respectively. This mode is invisible in the transmission spectra as well as in the DOS as the width of the resonance tends to zero. In addition to our analytical

prediction of the BIC position at $\Omega = 1$, different phenomena appear when we gradually shift the stub of length d_4 from $d_4 = 1$. Indeed, if we shift strongly d_4 from $d_4 = 1$ (for example, $d_4 = 0.5$), one can see [Fig. 7(a)] the existence of a broad transparency window squeezed between two dips indicated by solid and dashed vertical arrows. In this case, this phenomenon can be qualified as ATS effect. ATS is a transparency window squeezed between two dips, which is similar to the EIT profile in the transmission spectra but with different intrinsic mechanisms. The first dip indicated by the solid arrow remains almost fixed at $\Omega = 1$ whatever the value of d_4, while the second dip indicated by the dashed arrow depends considerably on d_4. For $d_4 = 0.7$ [Fig. 7(b)], the width of the transparency window between the two dips decreases, therefore, a transition between ATS and EIT occurs where the two phenomena coexist. Remarkably, near the BIC point [Fig. 7(c)], the second dip get even closer to the fixed
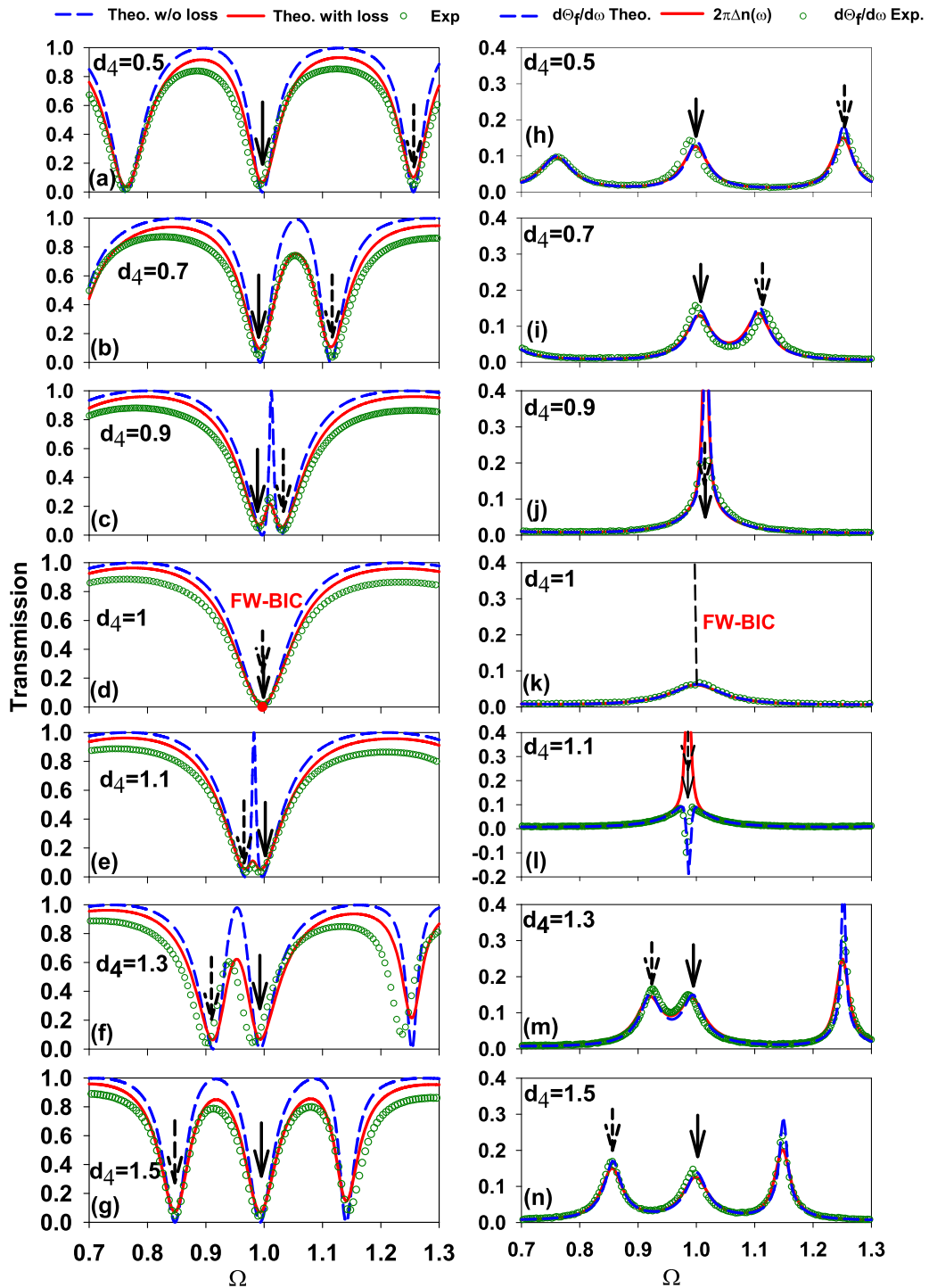
FIG. 7. (a)–(g) (Left panel) Transmission coefficient versus Ω for different values of d_4 around $d_4 = 1$. The lengths of the arms of the loop are taken such that $d_2 = 0.2$ and $d_3 = 1.8$. Blue and red curves correspond to theoretical results without and with loss, respectively, whereas green curves correspond to experimental results. (h)–(n) (Right panel) Variation of the DOS $\Delta n(\omega)$ (red lines) and the derivative of the Friedel phase $\frac{d\theta_f}{d\omega}$ (blue dashed curves) for different values of d_4. The theoretical results of $\frac{d\theta_f}{d\omega}$ (blue dashed lines) are validated by the experimental data (green open circles). The position of FW BIC is indicated by the filled circle in (d) and by dashed line in (k). The solid and dashed arrows indicate the positions of transmission dips associated to the two interacting modes of the DBCS.

dip at $\Omega = 1$ leading to the narrowing of the width of the transparency window between them. This is a characteristic of the EIT resonance. For $d_4 = 1$, the two dips cross each other at $\Omega = 1$ and the width of the resonances collapses to

a hidden resonance or BIC with an infinite lifetime as shown in Fig. 7(d). The same behavior occurs for $d_4 > 1$ where the second dip reappears again but at the left-hand side of the fixed dip (i.e., $\Omega < 1$) as shown in Figs. 7(e)–7(g).

These behaviors are confirmed also in the DOS (red lines) and the derivative of the Friedel phase $\frac{d\theta_f}{d\omega}$ (dashed blue lines) in Figs. 7(h)–7(n) (left panel) which provides a deeper understanding of the FW BIC. The BIC appears as a delta peak in the DOS [Fig. 7(k)] with an infinite lifetime, whereas, by detuning from the BIC condition, the dips appear as classical Breight-Wigner resonances characterized by a given width related to their lifetime. From the DOS spectra, one can see that the first resonance which corresponds to the first dip in the transmission spectra remains almost fixed around $\Omega = 1$, while the second resonance is strongly affected by d_4. The position and width of the peak decrease [Fig. 7(i)] and merge with the first resonance for $d_4 = 0.9$ [Fig. 7(j)]. For $d_4 = 1$ [Fig. 7(k)], the width of one of the two resonances vanishes giving rise to a delta peak at $\Omega = 1$ which corresponds to FW BIC, whereas the second resonance becomes broader and more lossy. For $d_4 > 1$ [Figs. 7(l)–7(n)], the same behavior appears where the second resonance reappears this time below the first one at $\Omega < 1$. A comparative study of DOS (red lines) and $\frac{d\theta_f}{d\omega}$ (blue dashed lines) is illustrated in Figs. 7(h)–7(n). One can notice that around the BIC position, the DOS and $\frac{d\theta_f}{d\omega}$ exhibit different behavior around $\Omega = 1$ for $d_4 = 1.1$ where $\frac{d\theta_f}{d\omega}$ presents negative delta peak at the quasi-BICs. Whereas, when we shift far from $d_4 = 1$, the DOS becomes almost similar to $\frac{d\theta_f}{d\omega}$.

C. Discerning EIT from ATS

It is well known that there is a common feature between EIT and ATS. Both phenomena involve the transmission zeros which are induced by the coupling field. When the coupling field is strong so that the two transmission zeros are well separated, then ATS is obtained. Whereas, in the case of a weak coupling field, the two transmission zeros get close to each other, and EIT appears due to the interference between the incident wave and scattered wave. The formation of the transparency window exists because of the superposition of two Lorentzian profiles representing the two transmission zeros (two dips). However, in order to quantitatively discriminate EIT from ATS, an AIC test is used to fit our theoretical data and to choose the best explanation for the induced transparency window in each coupling regime. Aside from the different mechanisms associated to ATS and EIT, analytical fitting methods [46,52,67] have been proposed to distinguish between EIT and ATS. The fitting formula for ATS can be written as [52]

$$T_{\text{ATS}} = 1 - \frac{C_1(\Gamma_1/2)^2}{(\Omega - \Omega_1)^2 + (\Gamma_1/2)^2} - \frac{C_2(\Gamma_2/2)^2}{(\Omega - \Omega_2)^2 + (\Gamma_2/2)^2},$$ (29)

where Ω_1 and Ω_2 are the dimensionless frequencies corresponding to the two dips, and C_1, C_2, Γ_1, and Γ_2 are free parameters to fit with the theoretical data. The signs of the second and the third terms are both negative. Similarly, the fitting formula of EIT is given by[52]

$$T_{\text{EIT}} = 1 - \frac{C_+(\Gamma_+/2)^2}{(\Omega - \Omega_c - \epsilon)^2 + (\Gamma_+/2)^2}$$
$$+ \frac{C_-(\Gamma_-/2)^2}{(\Omega - \delta_c)^2 + (\Gamma_-/2)^2},$$ (30)

where Ω_c is the dimensionless frequency corresponding to the peak, and C_+, C_-, Γ_+, Γ_-, and ϵ are free parameters to fit with the theoretical data. Obviously, the opposite signs of the second and third terms cause destructive interference, giving rise to a transparency window in the shape of EIT resonance. By using the least-squares method to fit the transmission coefficients in Eqs. (29) and (30) with the theoretical data, it is recommended to consider the physical meaning of the free parameters to set reasonable initial values, where C_1, C_2, C_+, and C_- are the amplitudes of the Lorentzian profiles, Γ_1, Γ_2, Γ_+, and Γ_- are their full width at half-maximum (FWHM), and ϵ is the shift from Ω_c with a small value.

In Fig. 8, we have compared directly our theoretical transmission spectra (black lines) with the fit functions ATS (blue curves) and EIT (red curves) for three values of d_4 as illustrated in Figs. 8(a)–8(c). In the case $d_4 = 0.5$ [Fig. 8(a)], where the ATS effect is predominant, the fitting curves using ATS formula [Eq. (29)] match very well with the theoretical data where the peaks and dips are well reproduced. In contrast, as expected, the fitting curves obtained with the EIT formula [Eq. (30)] fail to match the theoretical results (red curves). The good agreement for the ATS model supports the proposed physical mechanism that the ATS effect originates from the strong splitting between the two modes of the structure. For $d_4 = 0.7$ [Fig. 8(b)], the transmission spectrum deviates appreciably from both EIT and ATS models which can be explained by the transition region from EIT to ATS. Furthermore, in the case $d_4 = 0.9$ [Fig. 8(c)], the theoretical data fit very well with EIT model and deviate drastically from the ATS model. Note that when fitting the ATS model, the transparency window disappears, which means that the ATS model cannot ever be applied (blue curves).

By varying the stub of length d_4, the transition from ATS to EIT can be quantitatively studied by evaluating the quality of the fit models. The AIC is used to discern EIT from ATS, which provides a method to select the best model from a set of models quantifying the amount of information loss, i.e., the degree of unfitness, and is given as $I_j = 2k' - 2ln(L_j)$, where k' is the number of unknown parameters used in the fitting [46] and L_j is the maximum likelihood function for the candidate model A_j, i.e., $j = $ ATS or EIT. Since we already found the best-fit models of EIT and ATS, it is sufficient to calculate the relative likelihood of these two models. The relative likelihood of model A_j out of two models is measured by the relative weight as [46]

$$\overline{w}_{\text{ATS}} = \frac{e^{-I_{\text{ATS}}/2}}{e^{-I_{\text{ATS}}/2} + e^{-I_{\text{EIT}}/2}},$$ (31)

with $\overline{w}_{\text{ATS}} + \overline{w}_{\text{EIT}} = 1$.

Figures 8(d) and 8(e) show the AIC mean weight for ATS (blue curves) and EIT (red curves) models for three values of d_4. Figures 8(d) and 8(e) represent the AIC obtained by fitting the theoretical data without and with loss, respectively, whereas, Fig. 4(f) corresponds to the AIC obtained by fitting the experimental data. An analysis of Figs. 8(d) and 8(e) reveals, as expected, that the AIC mean weight of ATS model is dominant for $0.5 \leqslant d_4 \leqslant 0.65$, which means that the two dips are sufficiently separated and so the transmission spectrum behaves like two individual dips with a strong splitting effect. Whereas, when d_4 is around $d_4 = 1$ ($0.8 \leqslant d_4 \leqslant 0.98$ and
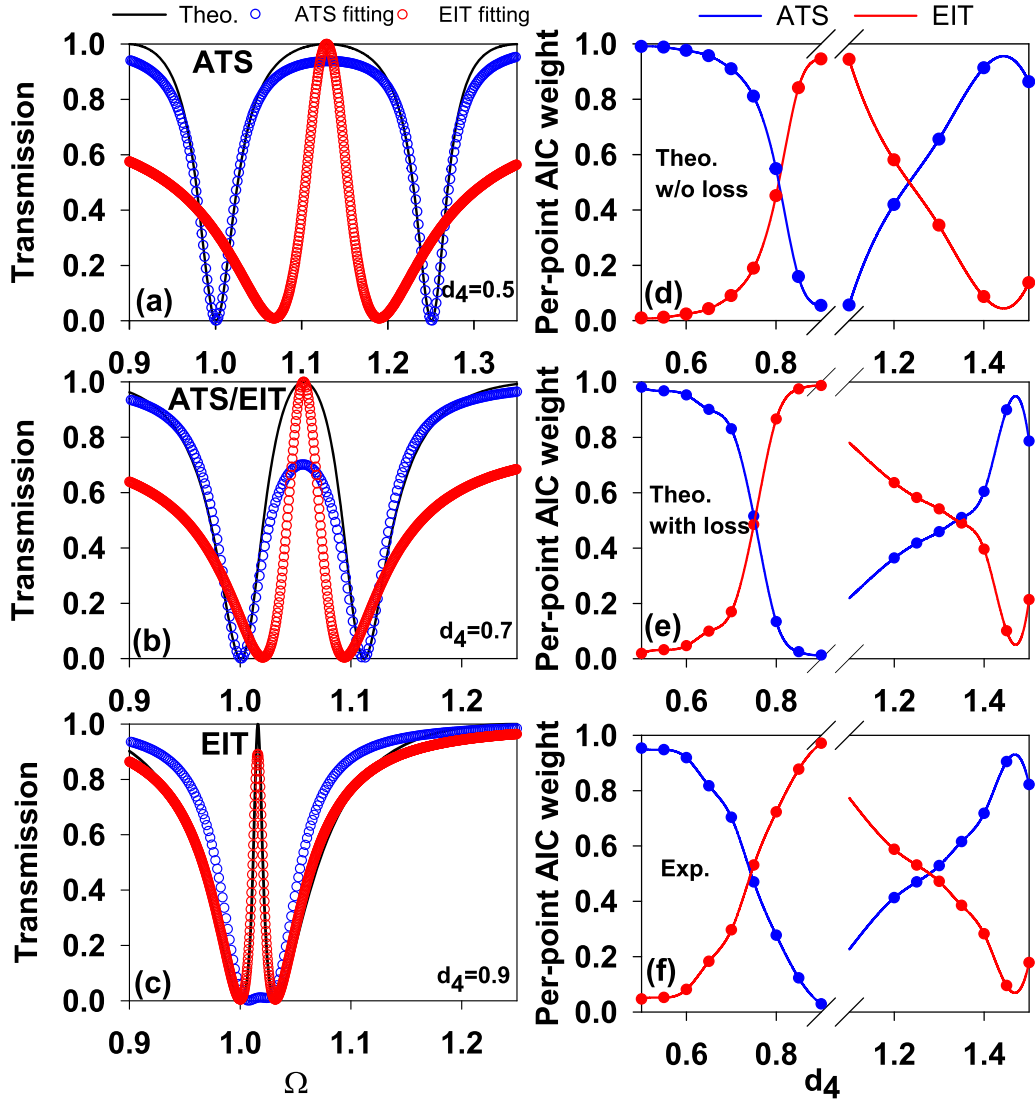
FIG. 8. Comparison of the fitting curves obtained with the ATS model (blue curves) and with the EIT model (red curves) with the theoretical results (black lines) for $d_4 = 0.5$ (a), 0.7 (b), and 0.9 (c). AIC per-point weight of the EIT and ATS models as a function of d_4 obtained by fitting the theoretical data without (d) and with (e) loss, and the experimental data (f).

$1.02 \leqslant d_4 \leqslant 1.2$), the separation becomes weak and the two dips get closer, then the EIT effect occurs, as shown by the increase in $\overline{w}_{EIT}$. However, when d_4 increases further, the AIC mean weight of ATS becomes dominant again for $1.4 \leqslant d_4 \leqslant 1.5$. We also notice that the system transits from EIT to ATS regime when d_4 is around 0.75 and 1.3. Note that the EIT and ATS coexist at these two crossing points. As mentioned above, for $d_4 = 1$, the two dips fall at the same value ($\Omega = 1$), then the width of the resonance vanishes giving rise to a FW BIC. A good agreement is obtained between the theoretical [Fig. 8(e)] and experimental [Fig. 8(f)] AIC weights.

Let us mention that the previous results can also be obtained with the coupling of two modes of NBCS and one mode of DBCS. In this case, we shall set the length of the wire d_1 to $d_1 = 1$. The details of these calculations and some illustrations of dispersion relations are given in the Supplemental Material SM2 [70]. Also, a detailed study about the effect of the wire of length d_1 on EIT and EIR resonances is also provided in the Supplemental Material SM3 [70].

IV. BICS AND RESONANCES INDUCED BY THE TWO ARMS OF THE LOOP

In Sec. II B [Eq. (15)], we have shown the existence of BICs when d_2 and d_3 are taken commensurate (i.e., $\frac{d_2}{d_3} = \frac{m_2}{m_3}$ where m_2 and m_3 have the same parity). These BICs are independent of d_1 and d_4. In what follows, we shall focus on the BICs around $d_2 = d_3$ (i.e., $m_2 = m_3 = 1$) and introduce the detuning $\Delta = \frac{d_2 - d_3}{2}$. Similarly to Eq. (25), Eqs. (3) and (4) can be written more appropriately for the discussions below as follows:

$$\tau = S\{2C_4(2S_1 S - C_1 C) + S_4(2CS_1 + C_1 S)\} - C_1 S_4 \sin^2(k\Delta) \tag{32}$$

and

$$\rho = S\{2C_4(2C_1 S + S_1 C) + S_4(2CC_1 - S_1 S)\} + S_1 S_4 \sin^2(k\Delta). \tag{33}$$

In particular, if $\Delta = 0$ (i.e., $d_2 = d_3$), we obtain a decoupling between the modes of DBCS given by Eq. (34),

namely,

$$S = 0 \qquad (34)$$

or

$$2C_4(2S_1S - C_1C) + S_4(2CS_1 + C_1S) = 0. \qquad (35)$$

Similarly, the modes of NBCS which are given by Eq. (33) divided into two totally decoupled sets given by

$$S = 0 \qquad (36)$$

or

$$2C_4(2C_1S + S_1C) + S_4(2CC_1 - S_1S) = 0. \qquad (37)$$

The above analysis shows that the modes given by $S = 0$ (i.e., $kd = m\pi$, m is a nonzero integer) are common modes of $\tau = 0$ [Eq. (32)] and $\rho = 0$ [Eq. (33)], respectively, and therefore present BICs whatever the values of d_1 and d_4.

The crossing between the modes given by Eqs. (34) and (35) of the DBCS occurs for $d_1 = m_1$ (m_1 is an integer). Similarly, the crossing of the modes given by Eqs. (36) and (37) of the NBCS occurs for $d_1 = m_1' + \frac{1}{2}$ (m_1' is an integer). An example of the crossing of the two decoupled branches of the DBCS around $d_1 = 1$ ($m_1 = 0$) and $\Omega = 1$ (i.e., $m = 1$) for $\Delta = 0$ is given in Fig. 9(a) (green curves) for $d_4 = 0.5$. The horizontal branch at $\Omega = 1$ corresponds to the BIC induced by the loop [Eq. (34)], the other branch is given by Eq. (35). For $\Delta \neq 0$, the term on the right-hand side of Eq. (32) plays the role of the coupling parameter which enables a lifting of the degeneracy of the two crossing branches obtained for $\Delta = 0$. An example is given in Fig. 9(a) for $\Delta = 0.1$ (dark red curves) with $\kappa = 0.12$. κ increases almost linearly as a function of Δ as it is shown in Fig. 9(b). Figures 9(c) and (d) show the dispersion curves of both DBCS (cyan curves) and NBCS (pink curves) for $\Delta = 0$ and 0.1, respectively. As predicted from Eqs. (34) and (36), both types of modes in Fig. 9(c) exhibit a common horizontal branch at $\Omega = 1$ giving rise to a robust BIC whatever the value of d_1. For $\Delta = 0.1$ [Fig. 9(d)], an avoided crossing between the modes appears around $d_1 = 1$ for DBCS and around $d_1 = 0.5, 1.5$ for NBCS. At the lifting of the degeneracy of the DBCS modes at $d_1 = 1$ and $\Omega = 1$ (cyan curves), there exists an NBCS mode between them (pink curve). This is a characteristic of the EIT resonance as shown in Figs. 9(e) and 9(f) where we plotted the transmission spectra versus Ω for $\Delta = 0$ and 0.1, respectively. For $\Delta = 0$ [Fig. 9(e)], one can observe the existence of FW BIC at $\Omega = 1$. When Δ deviates from $\Delta = 0$ [Fig. 9(f)], the FW BIC transforms to EIT resonance. Similarly, at the lifting of the degeneracy of the NBCS modes at $d_1 = 0.5$ and 1.5 around $\Omega = 1$ (pink curves), there exists a DBCS mode (cyan curve). This is a characteristic of the EIR resonance as shown in Figs. 9(g) and 9(h).

The variation of the transmission magnitude spectra in presence of loss is reported in Figs. 10(a) and 10(b) (in color scale) for $\Delta = 0$ and 0.1, respectively. We have indicated by horizontal line the position of the BIC in Fig. 10(a) for $\Delta = 0$. These modes are not visible in the transmission spectra and remain robust whatever the value of d_1 (indicated by the large circles). By slightly detuning Δ from 0 [Fig. 10(b)], a thin transparency window appears between the two transmission

zeros around $d_1 = 1$ giving rise to EIT resonance. These results are confirmed experimentally in Figs. 10(c) and 10(d) for $\Delta = 0$ and 0.1, respectively. Additionally, the phenomenon is inverted around $d_1 = 0.5$ and 1.5 (i.e., $m_1' = 0, 1$) where a transmission zero is squeezed between two transmission maxima; this is a characteristic of the EIR resonance as illustrated in Figs. 10(e)–10(h).

Now, we fix the values of d_1 and d_4 to 1 and 0.5, respectively, and we discuss the effect of the detuning $\Delta = \frac{d_2 - d_3}{2}$ between the two arms of lengths d_2 and d_3 of the loop. In this case, two types of BICs can be found as a function of Δ. Figure 11(a) shows the dispersion curves versus Δ for the DBCS (cyan curves) and NBCS (pink curves). The open circles represent the minima and maxima of the transmission coefficient extracted from the experimental data. The black diamonds indicate the position of the FW BICs marked I, II, III, and IV. Let us consider separately two regions: region of no coupling ($\kappa = 0$) and region of coupling ($\kappa \neq 0$). The former occurs at $\Omega = 1$ where the dispersion curves cross each other, resulting in the formation of FW BIC marked I and II. The corresponding coordinates are ($\Delta_{\text{I}} = 0$, $\Omega_{\text{I}} = 1$) and ($\Delta_{\text{II}} = 1$, $\Omega_{\text{II}} = 1$). These modes are obtained analytically from Eq. (15) (i.e., $\Omega = \frac{m_2 + m_3}{2}$ and $\Delta = \frac{m_2 - m_3}{m_2 + m_3}$ with $m_2 = m_3 = 1$ and $m_2 = 2$, $m_3 = 0$ respectively). When we move away from the crossing points, we assist to a separation between the two modes of the DBCS. Now, around $\Delta_{\text{III}} = 0.4$ and $\Delta_{\text{IV}} = 0.68$, the modes undergo a strong coupling accompanied by a typical anticrossings with Rabi splitting $\kappa = 0.085$ and 0.075, respectively. Therefore, the FW BICs marked III appear on the upper branch around $\Omega_{\text{III}} = 1.3$ and marked on the lower branch IV around $\Omega_{\text{IV}} = 0.73$ where the modes of DBCS and NBCS intersect. These latter BICs are obtained graphically from Eq. (14). However, a separation between the two modes (DBCS and NBCS) occurs outside the anticrossing regions.

The variation of the transmission magnitude (in color scale) versus Ω and Δ is given in Fig. 11(b), demonstrating the crossing points with $\kappa = 0$ at $\Omega = 1$, $\Delta_{\text{I}} = 0$, and $\Delta_{\text{II}} = 1$. Also, one can see the regions of the coupling where the anticrossings are observed with $\kappa = 0.085$ and 0.075 around $\Delta_{\text{III}} = 0.4$ and $\Delta_{\text{IV}} = 0.68$, respectively. Furthermore, there are two remarkable common features of the two regimes in Fig. 11(b). First, it can be clearly noticed that one mode takes all losses (i.e., $\gamma_+ = \gamma_1 + \gamma_2$) while the other mode becomes a BIC (i.e., $\gamma_- = 0$). Second, when we shift from these specific points, one can obtain a transparency window squeezed between two transmission zeros giving rise to EIT resonances. The theoretical results [Fig. 11(b)] are in good agreement with the experimental results [Fig. 11(c)]. In Figs. 11(d)–11(f), we plotted the calculated and measured transmission spectra around the anticrossing point at ($\Delta_{\text{III}} = 0.4$, $\Omega_{\text{III}} = 1.3$). Figure 11(e) shows the position of the FW BIC marked III for $\Omega_{\text{III}} = 1.3$ and $\Delta_{\text{III}} = 0.4$. Around $\Delta_{\text{III}} = 0.4$, the FW BIC transforms to EIT resonance as shown in Figs. 11(d) and 11(f) for $\Delta = 0.3$ and 0.5, respectively. One can also observe that the width of the transparency window increases when Δ shifts away from the anticrossing point. The behavior of the transmission spectra around the BICs marked I and II has been already discussed in Fig. 9(e). It is worth noting that the coupling between the modes of the cavity around $\Omega = 1$
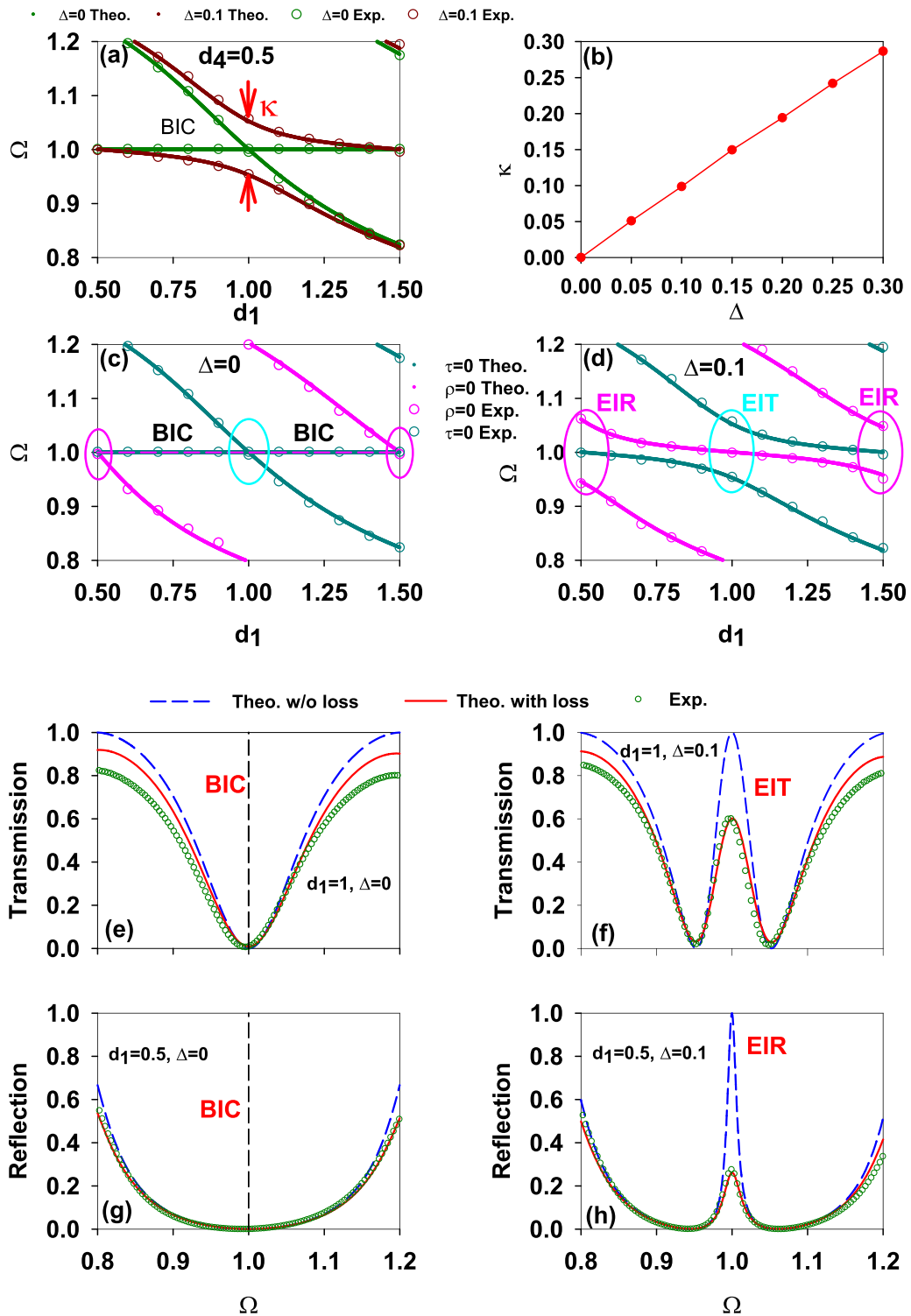
FIG. 9. (a) Dispersion curves of DBCS versus the length d_1 for $\Delta = 0$ (green curves) and $\Delta = 0.1$ (dark red curves). (b) Rabi splitting κ between the two modes in (a) as a function of Δ. Dispersion curves of both DBCS (cyan curves) and NBCS (pink curves) as a function of d_1 for (c) $\Delta = 0$ and (d) $\Delta = 0.1$. Variation of the transmission magnitude versus Ω and d_1 for (e) $\Delta = 0$ and (f) $\Delta = 0.1$ in the case d_1. Variation of the reflection magnitude versus Ω for (g) $\Delta = 0$ and (h) $\Delta = 0.1$ in the case $d_1 = 0.5$. The horizontal dashed line in (e) indicates the position of the robust BIC. The large circles indicate the positions of crossing and anticrossing points.
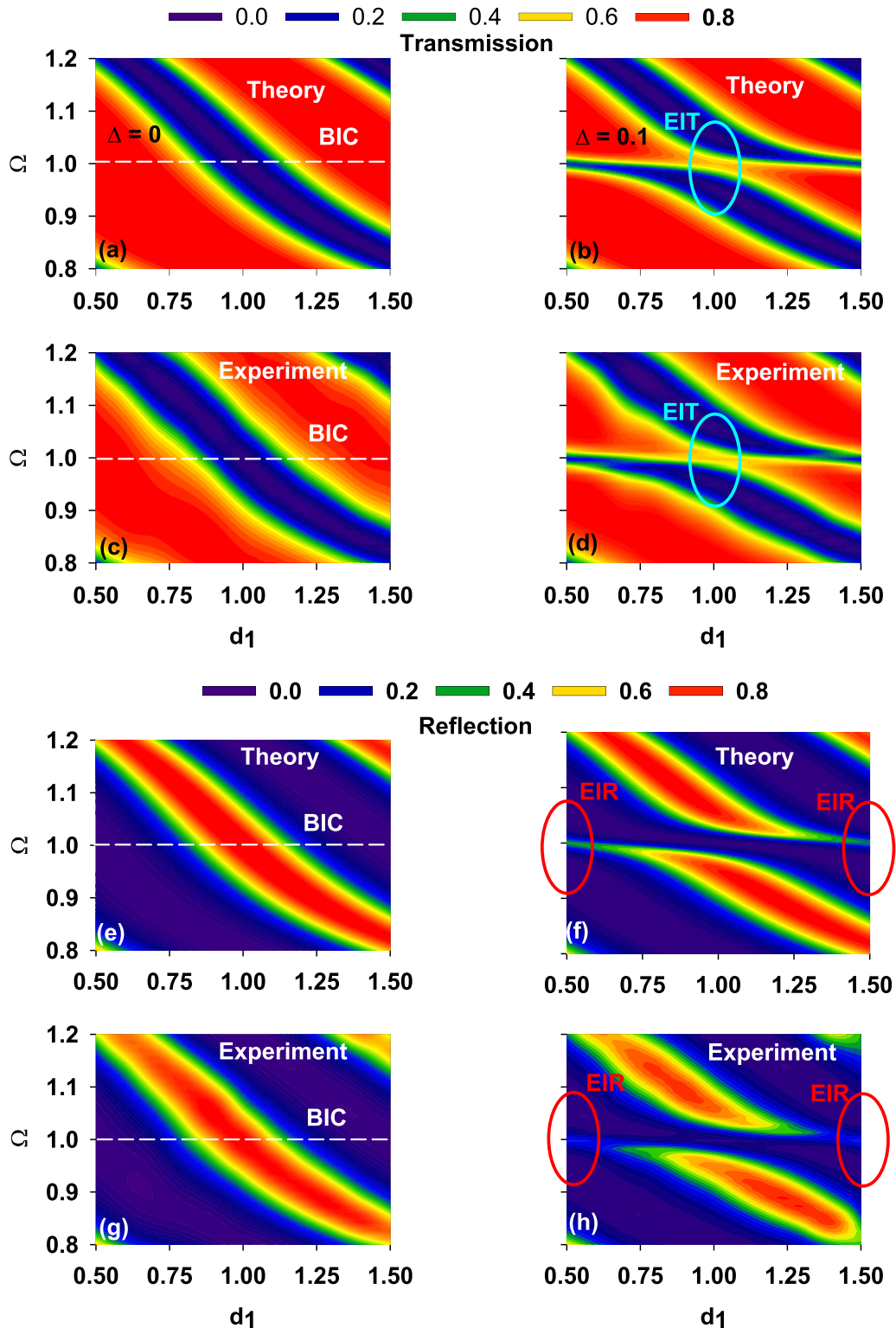
FIG. 10. Variation of the transmission magnitude versus Ω and d_1 for (a) $\Delta = 0$ and (b) $\Delta = 0.1$. The horizontal dashed line in (a) indicates the position of the robust BIC. (c), (d) Experimental validation of the results in (a) and (b), respectively. Variation of the reflection magnitude versus Ω and d_1 for (e) $\Delta = 0$ and (f) $\Delta = 0.1$. (g), (h) Experimental validation of the results in (e) and (f), respectively. The large cyan and red circles indicate the positions of EIT and EIR resonances, respectively.

depends significantly on d_4. Indeed, when $d_4 \neq 0.5$, we assist to a lifting of degeneracy at the crossing points giving rise to anticrossing points (not shown here).

All the analytical results presented in Sec. II B about the BIC analysis remain valid when the boundary condition at the end of the stub of length d_4 is $E = 0$ (i.e., vanishing electric
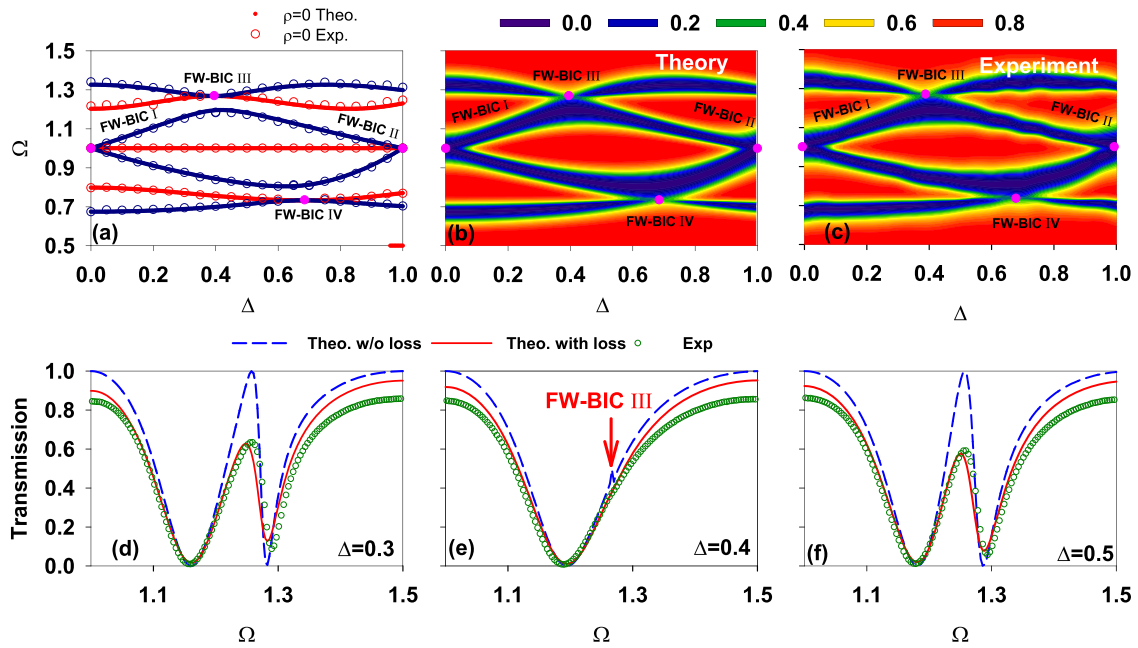
FIG. 11. Dispersion curves of DBCS (cyan curves) and NBCS (pink curves) as a function of Δ for $d_1 = 1$ and $d_4 = 0.5$. (b), (c) Variation of the theoretical and experimental transmission magnitude versus Ω and Δ, respectively. The black diamonds show the positions of FW BICs. (d)–(f) Transmission spectra for three values of Δ around $\Delta = 0.4$ and $\Omega = 1.3$. Blue and red curves correspond to the theoretical results without and with loss, respectively, whereas green circles correspond to experimental data.

field) instead of $H = 0$. Just we need to permute C_4 by $-S_4$ and S_4 by $-C_4$ in all equations.

V. CONCLUSION

In summary, we have given an analytical and experimental evidence about the existence of FW BICs in a simple cavity made of a loop of length $2d = d_2 + d_3$ connected to a stub of length d_4. The whole cavity is attached vertically to two semi-infinite waveguides by a wire of length d_1. The behavior of FW BICs is analyzed as a function of several geometrical parameters constituting the cavity. Indeed, we have shown the existence of FW BICs induced by (i) the loop and the stub, in particular when d_4 and d are taken appropriately commensurate at certain frequencies whatever the value of d_1, d_2, and d_3. By slightly deviating d_4 from the corresponding conditions, one can obtain either EIT or ATS depending on the values of d_4. Due to the similarity of the transparency window in the transmission spectra, ATS and EIT phenomena are first fitted with the corresponding analytical expressions, where the difference between both phenomena is highlighted. The fit parameters are demonstrated as function of the length of the stub d_4. Based on the AIC criterion, we have clearly

identified the EIT and ATS regimes as well as the transition from ATS regime to EIT regime. In addition, there exist other types of FW BIC which are associated to the loop-stub system whatever the value of d_1. The geometrical parameters and the corresponding frequencies are obtained graphically. (ii) When d_2 and d_3 are taken commensurate, one can obtain a FW BIC whatever the values of d_1 and d_4 and which transforms into EIT, EIR, or ATS resonances when we shift slightly from the BIC condition. Also, we have given an experimental determination of the DOS through an analysis of the argument of the determinant of the scattering matrix. This study has been performed by means of the Green's function method which enables us to determine analytically the transmission and reflection coefficients as well as the dispersion relations and DOS. The analytical results are confirmed by the experimental measurements using the coaxial cables in the radio-frequency regime. The results presented in this work can be transposed straightforwardly to mesoscopic systems [11,12,80] as well as plasmonic MIM waveguides operating in the infrared domain by taking properly the geometrical parameters at the nanoscale [22,81]. The structure can be proposed to realize an efficient refractive index sensor. This last work is in progress.

[1] M. V. Rybin, K. L. Koshelev, Z. F. Sadrieva, K. B. Samusev, A. A. Bogdanov, M. F. Limonov, and Y. S. Kivshar, High-Q Supercavity Modes in Subwavelength Dielectric Resonators, Phys. Rev. Lett. **119**, 243901 (2017).

[2] J. Von Neumann and E. P. Wigner, Uber merkwiirdige diskrete Eigenwerte, Phys. Z. **30**, 465 (1929).

[3] R. Parker, Resonance effects in wake shedding from parallel plates: calculation of resonant frequencies, J. Sound Vib. **5**, 330 (1967)

[4] D. Evans and R. Porter, Trapped modes embedded in the continuous spectrum, Q. J. Mech. Appl. Math. **51**, 263 (1998).

[5] C. M. Linton, M. McIver, P. McIver, K. Ratcliffe, and J. Zhang, Trapped modes for off-centre structures in guides, Wave Motion **36**, 67 (2002).

[6] Y. Duan, W. Koch, C. Linton, and M. McIVER, Complex resonances and trapped modes in ducted domains, J. Fluid Mech. **571**, 119 (2007).

[7] S. Hein, and W. Koch, Acoustic resonances and trapped modes in pipes and tunnels, J. Fluid Mech. **605**, 401 (2008).

[8] A. A. Lyapina, D. N. Maksimov, A. S. Pilipchuk, and A. F. Sadreev, Bound states in the continuum in open acoustic resonators, J. Fluid Mech. **780**, 370 (2015).

[9] L. Huang, Y. K. Chiang, S. Huang, C. Shen, F. Deng, Y. Cheng, B. Jia, Y. Li, D. A. Powell, and A. E. Miroshnichenko, Sound trapping in an open resonator, Nat. Commun. **12**, 4819 (2021).

[10] M. Amrani, I. Quotane, C. Ghouila-Houri, E. H. El Boudouti, L. Krutyansky, B. Piwakowski, P. Pernod, A. Talbi, and B. Djafari-Rouhani, Experimental Evidence of the Existence of Bound States in the Continuum and Fano Resonances in Solid-Liquid Layered Media, Phys. Rev. Applied **15**, 054046 (2021).

[11] T. Mrabti, Z. Labdouti, A. Mouadili, E. H. El Boudouti, and B. Djafari-Rouhani, Aharonov-Bohm-effect induced transparency and reflection in mesoscopic rings side coupled to a quantum wire, Phys. E (Amsterdam) **116**, 113770 (2020).

[12] T. Mrabti, Z. Labdouti, O. El Abouti, E. H. El Boudouti, F. Fethi, and B. Djafari-Rouhani, Transmission gaps, trapped modes and Fano resonances in Aharonov-Bohm connected mesoscopic loops, Phys. Lett. A **382**, 613 (2018).

[13] F. He, J. Liu, G. Pan, F. Shu, X. Jing, and Z. Hong, Analogue of Electromagnetically Induced Transparency in an All-Dielectric Double-Layer Metasurface Based on Bound States in the Continuum, Nanomaterials **11**, 2343 (2021)

[14] Q. Mi, T. Sang, Y. Pei, C. Yang, S. Li, Y. Wang, and B. Ma, High-quality-factor dual-band Fano resonances induced by dual bound states in the continuum using a planar nanohole slab, Nanoscale Res. Lett. **16**, 150 (2021).

[15] S. I. Azzam and A. V. Kildishev, Photonic bound states in the continuum: From basics to applications, Adv. Opt. Mater. **9**, 2001469 (2021).

[16] S. Sun, Y. Ding, H. Li, P. Hu, C.-W. Cheng, Y. Sang, F. Cao, Y. Hu, A. Alù, D. Liu, Z. Wang, S. Gwo, D. Han, and J. Shi, Tunable plasmonic bound states in the continuum in the visible range, Phys. Rev. B **103**, 045416 (2021)

[17] Z. Qi, G. Hu, B. Liu, Y. Li, C. Deng, P. Zheng, F. Wang, L. Zhao, and Y. Cui, Plasmonic nanocavity for obtaining bound state in the continuum in silicon waveguides, Opt. Express **29**, 9312 (2021).

[18] S. Xie, S. Xie, J. Zhan, C. Xie, G. Tian, Z. Li, and Q. Liu, Bound States in the Continuum in a T-Shape Nanohole Array Perforated in a Photonic Crystal Slab, Plasmonics **15**, 1261 (2020).

[19] A. Kodigala, T. Lepetit, Q. Gu, B. Bahari, Y. Fainman, and B. Kanté, Lasing action from photonic bound states in continuum, Nature (London) **541**, 196 (2017).

[20] L. L. Doskolovich, E. A. Bezus, and D. A. Bykov, Integrated flat-top reflection filters operating near bound states in the continuum, Photon. Res. **7**, 1314 (2019).

[21] X. Cui, H. Tian, Y. Du, G. Shi, and Z. Zhou, Normal incidence filters using symmetry-protected modes in dielectric subwavelength gratings, Sci. Rep. **6**, 36066 (2016).

[22] M. Amrani, S. Khattou, Y. Rezzouk, A. Mouadili, A. Noual, E. H. El Boudouti, and B. Djafari-Rouhani, Analytical and numerical study of T-shaped plasmonic demultiplexer based on Fano and induced transparency resonances, J. Phys. D: Appl. Phys. **55**, 075106 (2022).

[23] F. Wu, J. Wu, Z. Guo, H. Jiang, Y. Sun, Y. Li, J. Ren, and H. Chen, Giant Enhancement of the Goos-Hänchen Shift Assisted by Quasibound States in the Continuum, Phys. Rev. Applied **12**, 014028 (2019).

[24] D. Conteduca, I. Barth, G. Pitruzzello, C. P. Reardon, E. R. Martins, and T. F. Krauss, Dielectric nanohole array metasurface for high-resolution nearfield sensing and imaging. Nat. Commun. **12**, 3293 (2021).

[25] C. W. Hsu, B. Zhen, A. D. Stone, J. D. Joannopoulos, and M. Soljačić, Bound states in the continuum, Nat. Rev. Mater. **1**, 16048 (2016).

[26] S. Li, C. Zhou, T. Liu, and S. Xiao, Symmetry-protected bound states in the continuum supported by all-dielectric metasurfaces, Phys. Rev. A **100**, 063803 (2019).

[27] Z. F. Sadrieva, M. A. Belyakov, M. A. Balezin, P. V. Kapitanova, E. A. Nenasheva, A. F. Sadreev, and A. A. Bogdanov, Experimental observation of a symmetry-protected bound state in the continuum in a chain of dielectric disks, Phys. Rev. A **99**, 053804 (2019).

[28] Y. Plotnik, Or Peleg, F. Dreisow, M. Heinrich, S. Nolte, A. Szameit, and M. Segev, Experimental Observation of Optical Bound States in the Continuum, Phys. Rev. Lett. **107**, 183901 (2011).

[29] S. Weimann, Y. Xu, R. Keil, A. E. Miroshnichenko, A. Tünnermann, S. Nolte, A. A. Sukhorukov, A. Szameit, and Y. S. Kivshar, Compact Surface Fano States Embedded in the Continuum of Waveguide Arrays, Phys. Rev. Lett. **111**, 240403 (2013).

[30] H. Friedrich and D. Wintgen, Interfering resonances and bound states in the continuum, Phys. Rev. A **32**, 3231 (1985).

[31] D. C. Marinica, A. G. Borisov, and S. V. Shabanov, Bound States in the Continuum in Photonics, Phys. Rev. Lett. **100**, 183902 (2008).

[32] E. N. Bulgakov and A. F. Sadreev, Bound states in the continuum in photonic waveguides inspired by defects, Phys. Rev. B **78**, 075105 (2008).

[33] A. F. Sadreev, Interference traps waves in an open system: bound states in the continuum, Rep. Prog. Phys. **84**, 055901 (2021).

[34] K. Koshelev, G. Favraud, A. Bogdanov, Y. Kivshar, and A. Fratalocchi, Nonradiating photonics with resonant dielectric nanostructures, Nanophotonics **8**, 725 (2019).

[35] A. A. Bogdanov, K. L. Koshelev, P. V. Kapitanova, M. V. Rybin, S. A. Gladyshev, Z. F. Sadriev, K. B. Samusev, Y. S. Kivshar, and M. F. Limonov, Bound states in the continuum and Fano resonances in the strong mode coupling regime. Adv. Photonics **1**, 016001 (2019).

[36] N. Solodovchenko, K. Samusev, D. Bochek, and M. Limonov, Bound states in the continuum in strong-coupling and weak-coupling regimes under the cylinder - ring transition, Nanophotonics **10**, 4347 (2021)

[37] S. Han, P. Pitchappa, W. Wang, Y. K. Srivastava, M. V. Rybin, and R. Singh, Extended bound states in the continuum with symmetry-broken terahertz dielectric metasurfaces, Adv. Opt. Mater. **9**, 2002001 (2021).

[38] M. Kang, S. Zhang, M. Xiao, and H. Xu, Merging Bound States in the Continuum at Off-High Symmetry Points, Phys. Rev. Lett. **126**, 117402 (2021).

[39] N. M. Shubin, A. V. Friman, V. V. Kapaev, and A. A. Gorbatsevich, Bound states in the continuum in asymmetrical quantum-mechanical and electromagnetic waveguides, Phys. Rev. B **104**, 125414 (2021).

[40] S. I. Azzam, V. M. Shalaev, A. Boltasseva, and A. V. Kildishev, Formation of Bound States in the Continuum in Hybrid Plasmonic-Photonic Systems, Phys. Rev. Lett. **121**, 253901 (2018).

[41] P. S. Pankin, B. R. Wu, J. H. Yang, K. P. Chen, I. V. Timofeev, and A. F. Sadreev, One-dimensional photonic bound states in the continuum, Commun. Phys. **3**, 91 (2020).

[42] U. Fano, Effects of configuration interaction on intensities and phase shifts, Phys. Rev. **124**, 1866 (1961).

[43] A. E. Miroshnichenko, S. Flach, and Y. S. Kivshar, Fano resonances in nanoscale structures, Rev. Mod. Phys. **82**, 2257 (2010).

[44] S. E. Harris, Electromagnetically induced transparency, Phys. Today **50**(7), 36 (1997).

[45] S. H. Autler and C. H. Townes, Stark effect in rapidly varying fields, Phys. Rev. **100**, 703 (1955).

[46] B. Peng, S. K. Ozdemir, W. Chen, F. Nori, and L. Yang, What is and what is not electromagnetically induced transparency in whispering-gallery microcavities, Nat. Commun. **5**, 5082 (2014).

[47] A. Rastogi, E. Saglamyurek, T. Hrushevskyi, S. Hubele, and L. J. LeBlanc, Discerning quantum memories based on electromagnetically-induced-transparency and Autler-Townes-splitting protocols, Phys. Rev. A **100**, 012314 (2019).

[48] Q. C. Liu, T. F. Li, X. Q. Luo, H. Zhao, W. Xiong, Y. S. Zhang, Z. Chen, J. S. Liu, W. Chen, F. Nori, J. S. Tsai, and J. Q. You, Method for identifying electromagnetically induced transparency in a tunable circuit quantum electrodynamics system, Phys. Rev. A **93**, 053838 (2016).

[49] J. Bai, J. Wang, S. Liu, J. He, and J. Wang, Autler Townes doublet in single photon Rydberg spectra of cesium atomic vapor with a 319 nm UV laser, Appl. Phys. B **125**, 33 (2019).

[50] Y. Jin, Y. Pennec, and B. Djafari-Rouhani, Acoustic analogue of electromagnetically induced transparency and Autler Townes splitting in pillared metasurfaces, J. Phys. D: Appl. Phys. **51**, 494004 (2018).

[51] P. M. Anisimov, J. P. Dowling, and B. C. Sanders, Objectively Discerning Autler-Townes Splitting from Electromagnetically Induced Transparency, Phys. Rev. Lett. **107**, 163604 (2011).

[52] L. Giner, L. Veissier, B. Sparkes, A. Sheremet, A. Nicolas, O. S. Mishina, M. Scherman, S. Burks, I. Shomroni, D. V. Kupriyanov, P. K. Lam, E. Giacobino, and J. Laurat, Experimental investigation of the transition between Autler-Townes splitting and electromagnetically-induced-transparency models, Phys. Rev. A **87**, 013823 (2013).

[53] C. Zhu, C. Tan, and G. Huang, Crossover from electromagnetically induced transparency to Autler-Townes splitting in open V-type molecular systems, Phys. Rev. A **87**, 043813 (2013).

[54] L. Y. He, T. J. Wang, Y. P. Gao, C. Cao, and C. Wang, Discerning electromagnetically induced transparency from Autler-Townes splitting in plasmonic waveguide and coupled resonators system, Opt. Express **23**, 23817 (2015).

[55] B. Wei and S. Jian, Objectively discriminating the optical analogy of electromagnetically induced transparency from Autler Townes splitting in a side coupled graphene-based waveguide system, J. Opt. **19**, 115001 (2017).

[56] B. Wei, G. Ren, and S. Jian, Crossover from plasmonic analogue of Fano resonance to Autler Townes splitting in a double guide mode resonances system, Appl. Phys. B **123**, 239 (2017).

[57] Y. Liu, A. Talbi, E. H. E. Boudouti, O. B. Matar, P. Pernod, and B. Djafari-Rouhani, Autler-Townes Splitting and Acoustically Induced Transparency Based on Love Waves Interacting with a Pillared Metasurface, Phys. Rev. Applied **11**, 064066 (2019).

[58] Y. Cheng, Y. Jin, Y. Zhou, T. Hao, and Y. Li, Distinction of Acoustically Induced Transparency and Autler-Townes Splitting by Helmholtz Resonators, Phys. Rev. Applied **12**, 044025 (2019).

[59] J. Liu, J. Wu, Y. Zhang, Y. He, and J. Zhang, Influence of dephasing on the Akaike information criterion distinguishing of quantum interference and Autler Townes splitting in coherent systems, J. Opt. Soc. Am. B **37**, 49 (2020).

[60] C. W. Hsu, B. Zhen, J. Lee, S. L. Chua, S. G. Johnson, J. D. Joannopoulos, and M. Soljacic, Observation of trapped light within the radiation continuum, Nature (London) **499**, 188 (2013).

[61] S. G. Lee, S. H. Kim, and C. S. Kee, Bound states in the continuum (BIC) accompanied by avoided crossings in leaky-mode photonic lattices, Nanophotonics **9**, 4373 (2020)

[62] T. Lepetit, E. Akmansoy, J.-P. Ganne, and J.-M. Lourtioz, Resonance continuum coupling in high-permittivity dielectric metamaterials, Phys. Rev. B **82**, 195307 (2010).

[63] S. Han, L. Cong, Y. K. Srivastava, B. Qiang, M. V. Rybin, A. Kumar, R. Jain, W. X. Lim, V. G. Achanta, S. S. Prabhu, Q. J. Wang, Y. S. Kivshar, and R. Singh, All-Dielectric Active Terahertz Photonics Driven by Bound States in the Continuum, Adv. Mater. **31**, 1901921 (2019)

[64] C. Kyaw, R. Yahiaoui, J. A. Burrow, V. Tran, K. Keelen, W. Sims, E. C. Red, W. S. Rockward, M. A. Thomas, A. Sarangan, I. Agha, and T. A. Searles, Polarization-selective modulation of supercavity resonances originating from bound states in the continuum, Commun. Phys. **3**, 212 (2020).

[65] S. Joseph, S. Sarkar, S. Khan, and J. Joseph, Exploring the optical bound state in the continuum in a dielectric grating coupled plasmonic hybrid system, Adv. Opt. Mater. **9**, 2001895 (2021).

[66] E. N. Bulgakov and D. N. Maksimov, Avoided crossings and bound states in the continuum in low-contrast dielectric gratings, Phys. Rev. A **98**, 053840 (2018)

[67] J. Liu, H. Yang, C. Wang, K. Xu, and J. Xiao, Experimental distinction of Autler-Townes splitting from electromagnetically induced transparency using coupled mechanical oscillators system, Sci. Rep. **6**, 19040 (2016).

[68] L. Dobrzynski, A. Akjouj, E. H. El Boudouti, G. Lévêque, H. Al-Wahsh, Y. Pennec, C. Ghouila-Houri, A. Talbi, B. Djafari-Rouhani, and Y. Jin, *Photonics*, Part II (Elsevier, Amsterdam, 2020).

[69] J. Friedel, The distribution of electrons around impurities in monovalent metals, Philos. Mag. **43**, 153 (1952).

[70] See Supplemental Material at http://link.aps.org/supplemental/10.1103/PhysRevB.106.125414 for the details on the analytical calculations based on the Green's function method (SM1), the dispersion relation of NBCS modes and some illustrations of the

solutions of DBCS and NBCS modes (SM2), and the effect of the wire of length d_1 on BICs, EIT, and EIR resonances (SM3).

[71] B. Djafari-Rouhani, E. H. El Boudouti, A. Akjouj, L. Dobrzynski, J. O. Vasseur, A. Mir, N. Fettouhi, and J. Zemmouri, Surface states in one-dimensional photonic band gap structures, Vacuum **63**, 177 (2001).

[72] M. Buttiker, Capacitance, admittance, and rectification properties of small conductors, J. Phys.: Condens. Matter **5**, 9361 (1993).

[73] H.-W. Lee, Generic Transmission Zeros and In-Phase Resonances in Time-Reversal Symmetric Single Channel Transport, Phys. Rev. Lett. **82**, 2358 (1999).

[74] A. Mouadili, E. H. El Boudouti, A. Soltani, A. Talbi, A. Akjouj, and B. Djafari-Rouhani, Theoretical and experimental evidence of Fano-like resonances in simple monomode photonic circuits, J. Appl. Phys. **113**, 164101 (2013).

[75] A. Mouadili, E. H. El Boudouti, A. Soltani, A. Talbi, B. Djafari-Rouhani, A. Akjouj, and K. Haddadi, Electromagnetically induced absorption in detuned stub waveguides: a simple analytical and experimental model, J. Phys.: Condens. Matter **26**, 505901 (2014).

[76] J. M. Bendickson, J. P. Dowling, and M. Scalora, Analytic expressions for the electromagnetic mode density in finite, one-dimensional, photonic band-gap structures, Phys. Rev. E **53**, 4107 (1996).

[77] M. L. H. Lahlaouti, A. Akjouj, B. Djafari-Rouhani, L. Dobrzynski, M. Hammouchi, E. H. El Boudouti, A. Nougaoui, and B. Kharbouch, Theoretical analysis of the density of states and phase times: Application to resonant electromagnetic modes in finite superlattices, Phys. Rev. B **63**, 035312 (2001).

[78] G. Gantzounis and N. Stefanou, Theoretical analysis of three-dimensional polaritonic photonic crystals Phys. Rev. B **72**, 075107 (2005).

[79] S. Khattou, M. Amrani, A. Mouadili, E. H. El Boudouti, A. Talbi, A. Akjouj, and Bahram Djafari-Rouhani, Comparison of density of states and scattering parameters in coaxial photonic crystals: Theory and experiment, Phys. Rev. B **102**, 165310 (2020).

[80] H. Al-Wahsh, A. Akjouj, B. Djafari-Rouhani, L. Dobrzynski, A. Mir, N. Fettouhi, M. Tij, and A. Bouzid, Quantum transport in one-dimensional monomode waveguides, Europhys. Lett. **57**, 711 (2002).

[81] A. Noual, O. El Abouti, El. El. Boudouti, A. Akjouj, Y. Pennec, and B. Djafari-Rouhani, Plasmonic-induced transparency in a MIM waveguide with two side-coupled cavities, Appl. Phys. A **123**, 49 (2017).